Failures in Detecting Volcanic Ash from a Satellite-Based Technique

James J. Simpson, Gary Hufford,† David Pieri,‡ and Jared Berg**

Immediate and accurate detection of airborne volcanic ash is an operational imperative of the aviation industry, especially jet aircraft. Ash encounters place passengers aboard these aircraft at severe risk and significantly impact, via forced rerouting, both the safety and profit margins of freight carriers due to their limited fuel supply. Moreover, the airlines can suffer high economic costs for repair and replacement of equipment. Operational detection and tracking of volcanic ash by most national weather services has relied heavily on a split window differencing technique of thermal longwave infrared channels on currently operational satellites. Unfortunately, prior work on volcanic ash detection has not emphasized the dynamical interaction between the erupting volcano and the effects of overlying atmospheric water vapor, phreatic and phreatomagmatic water sources. Six volcanic ash eruptions from around the globe were chosen for study because they have wide variation in ambient atmospheric water vapor, available ground and surface water and different magma types. Results show that the present differencing technique is not uniformly effective in properly classifying volcanic ash pixels in the satellite scene and often falsely interprets meteorological clouds as volcanic ash clouds and conversely. Moreover, it is not always a robust early detector, an operational aviation requirement. Seasonal variability in global integrated atmospheric water vapor, coupled with the geographical distribution of currently active volcanoes, suggests the concerns discussed herein with regard to six specific eruptions, have applicability to the global aviation industry. Operational implications are discussed and a strategic proposal is presented on necessary steps to improve detection. ©*Elsevier Science Inc., 2000*

INTRODUCTION

Importance of Volcanic Ash Detection

Airborne volcanic ash from violent eruptions is a major hazard to populations downwind both on the ground and in the air (Casadevall, 1994; Fox, 1988). In the past 15 years, more than 100 jet aircraft have been damaged owing to unexpected encounters. Passengers aboard many of those aircraft were put at severe risk and the airlines suffered high economic costs for repair and replacement (Casadevall, 1994). It is estimated that volcanic ash damage to commercial aircraft alone has been more than $250 million to date (personal communication, Airclaims, Ltd.). Moreover, the risk of airborne volcanic ash encounters may increase as the number of aircraft flying the world's air routes continues to rise.

Airborne volcanic ash encounters are compounded by the fact that volcanic ash clouds are not detectable by the present generation of radar instrumentation carried aboard aircraft and are not likely to be detectable in the foreseeable future. Complete avoidance is the only procedure that ensures flight safety (Campbell, 1994). Avoidance, however, is difficult because many of the eruptive volcanoes around the world are located in remote locations, are not instrumented, and are often near air traffic corridors. Detection methods for volcanic ash clouds must also be rapid and accurate so that aircraft can take immediate steps to avoid the ash cloud and continue to remain clear of it as the cloud drifts downwind.

Overview of Currently Used Detection Methods

Operational detection and tracking of volcanic eruption clouds have relied heavily on polar orbiter data [e.g., Advanced Very High Resolution Radiometer (AVHRR)]

---

* Scripps Institution of Oceanography, Digital Image Analysis Laboratory, University of California, La Jolla
† National Weather Service, Alaska Region, Anchorage, Alaska
‡ Jet Propulsion Laboratory, Pasadena, California

Address correspondence to J. J. Simpson, Scripps Inst. of Oceanography, Digital Image Analysis Lab., Univ. of California, La Jolla, CA 92093-0237. E-mail: jsimpson@ucsd.edu

Received 18 May 1999; revised 23 September 1999.

REMOTE SENS. ENVIRON. 72:191–217 (2000)

655 Avenue of the Americas, New York, NY 10010

0034-4257/00/$–see front matter
PII S0034-4257(99)00103-0

and/or geostationary satellite data [e.g., Geostationary Operational Environmental Satellite (GOES); the Japanese Geostationary Meteorological Satellite (GMS-5)]. The infrared channels on the AVHRR relevant to this study are the 10.3–to 11.3 μm (T_4) and the 11.5–12.5 μm (T_5) channels. The corresponding channels for GOES-8 and -10 are 10.2–11.2 μm (T_4) and 11.5–12.5 μm (T_5). For GMS-5, they are10.5–11.5 μm (T_4) and 11.5–12.5 μm (T_5). Operationally, relatively little use of the Total Ozone Mapping Spectrometer (TOMS) data has been made in this application. One reason for this lack of operational use is that TOMS data are restricted to daytime viewing. Nonetheless, TOMS data have been used successfully to calculate the mass of SO_2 in a volcanic cloud (Krueger et al., 1995; Schneider et al., 1999).

Two approaches have been used to detect volcanic ash with T_4 and T_5 brightness temperatures; a differencing of thermal infrared bands (T_4-T_5) or a ratio of these bands (T_4/T_5). The difference method assumes that volcanic clouds will produce negative T_4-T_5 differences whereas meteorological clouds will generally produce positive differences (Schneider and Rose, 1995). The ratio and difference methods assume that the reststrahlen effects from ash will produce a uniquely detectable signature in the T_4/T_5 ratio and the T_4-T_5 difference (Holasek and Rose, 1991). This latter assumption, however, is inconsistent with results reported by Prata (1989a,b) for the Galunggung eruption. He concluded that the thermal emission differences in the Galunggung plumes were associated with a reverse absorption effect due to acid particles and other volcanic debris in the plumes, rather than reststrahlen effects.

Schneider and Rose (1994) associated three types of clouds with the 1989–1990 Redoubt eruption in Alaska. Type 1 clouds are generated by magmatic explosions during the first week of activity and can extend hundreds of kilometers from the source vent. Type 2 clouds are generated in part by dome collapse and subsequent pyroclastic flows which occur within minutes of the eruption. Type 3 clouds are dispersed type 2 clouds and are imaged several hours after the eruption. Neither the difference nor the ratio algorithms were successful in detecting all three types of clouds. For type 1 clouds, the T_4-T_5 difference produced positive ΔT's for the proximal portion of the volcanic cloud and negative ΔT's for the distal portion. The T_4-T_5 difference produced positive ΔT's for both type 2 volcanic and weather clouds. The type 3 clouds were difficult to discriminate (Schneider and Rose, 1994).

Holasek and Rose (1991) performed a similar analysis on the 1986 Mt. Augustine eruption. In this case, they found the T_4/T_5 ratio test produced better detection than the T_4-T_5 difference test. These results, however, are critically dependent on the value of an assumed T_4/T_5 threshold. The threshold is not a constant; it depends strongly on the nature of the eruption.

Davies and Rose (1998) used a T_4-T_5 difference test on a sequence of GOES-8 images to detect the volcanic plume associated with the 1996 Montserrat eruption. The range of negative ΔT's used to detect the plume, however, also corresponds to the ΔT's associated with most of the meteorological clouds observed in these GOES images.

Purpose of This Article

Much of the prior work on volcanic ash detection has not emphasized the dynamical interaction between the erupting volcano and the overlying atmosphere. Moreover, little has been done to distinguish between a dry and wet eruption and the subsequent effect that these different types of eruptions can have on plume detection in satellite data. This article examines the effects of a variable atmosphere and of wet versus dry eruptions on volcanic plume detection. Then, results obtained by the current operational T_4-T_5 detection method, applied to specific eruptions studied herein, are generalized to the global distribution of active volcanoes.

DATA

Satellite Data

Full resolution GOES-8 data in McIDAS format were received from the National Climatic Data Center (NCDC) and converted to the Visual Information File Format (VIFF) for easy use in a UNIX workstation environment (Simpson and Al-Rawi, 1996). The scenes were sectorized to produce full resolution subsections around Montserrat. A 4-day time series, which brackets the 18 September 1996 Montserrat eruption, was processed at full spatial and digital resolution. Oversampling in the sample direction of the raw GOES data (count domain) was removed. Counts were retained for those analyses that required them. The GOES data also were calibrated to geophysical units using procedures developed by Weinreb et al. (1997).

GOES data for the Popocatepetl eruption were received as subsections from the U.S. Geological Survey (USGS). USGS calibrated these data to geophysical units and then remapped the data to a Lambert azimuthal projection. A 2-day time series for Popocatepetl, which brackets the 10–11 March 1996 eruption, was also processed at full spatial and digital resolution.

Data from GMS-5 were obtained from USGS and used to produce a high temporal resolution sequence of the Ruapehu eruption (16–17 June 1996). These data were processed in a manner similar to that used for GOES data, except there is no oversampling of GMS-5 data in the sample direction. Full resolution AVHRR data for the Mt. Augustine 28–30 March 1986, the Mt. Spurr/Crater Peak 19 August 1992, and the Ruapehu 16–17 June 1996 eruptions were received as subsections

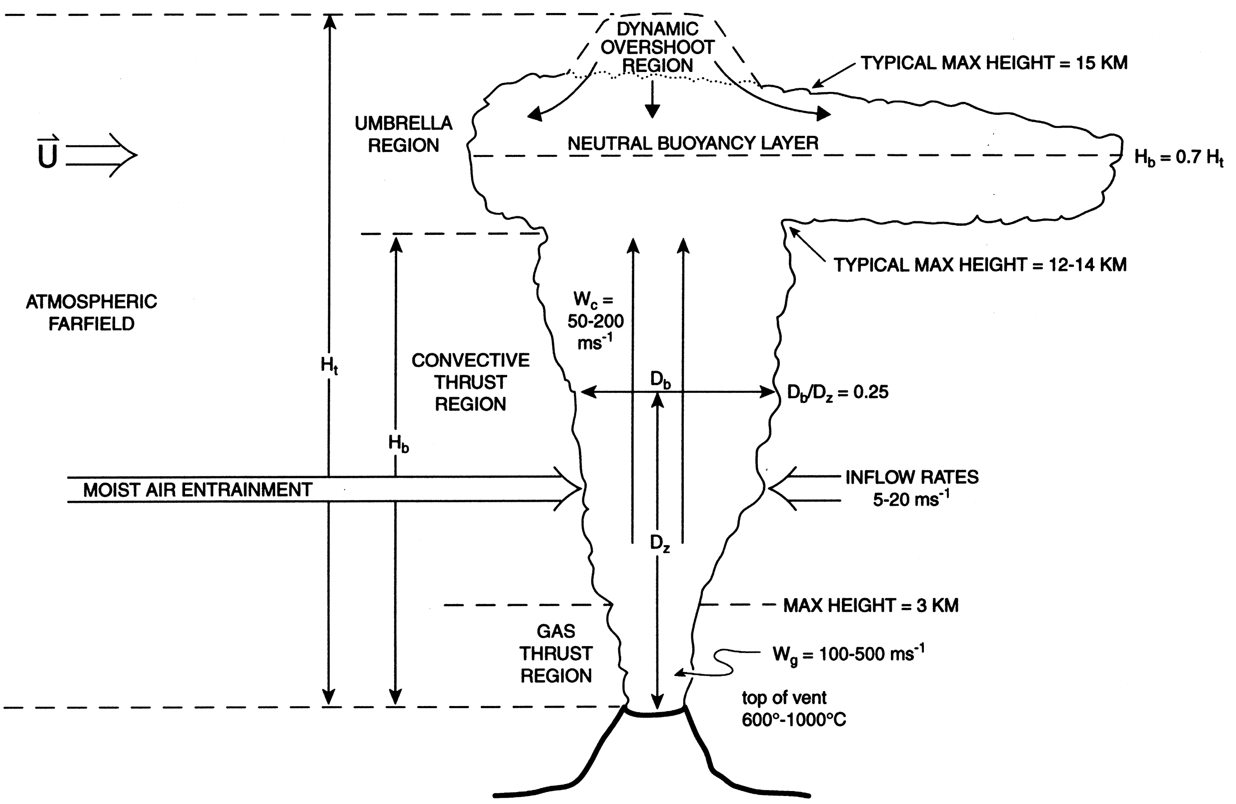

Figure 1. Conceptual model of volcanic–atmosphere interaction. See text for details.

from the USGS. USGS calibrated these data to geophysical units using procedures recommended by NOAA (NOAA/NESDIS Technical Memorandum 107, 1979 and updates) and then remapped the data to a Lambert azimuthal projection. GAC resolution AVHRR data for Rabaul were received from NCDC in NOAA-1B format and converted to the VIFF format. Processing was done using the TIGRIS system (Simpson and Al-Rawi, 1996)

Radiosonde Data

Measurements of the upper atmosphere are obtained from radiosondes. A radiosonde is a radio-equipped instrument package borne aloft by a balloon. The instrument transmits profiles of temperature, pressure, and relative humidity up to an altitude of about 30 km. In addition, winds at various levels are computed by tracking the balloons with a radio direction-finding antenna. Worldwide observations are collected twice each day at 0000 and 1200 UTC. From these data, a number of thermodynamic variables can be computed (Houghton, 1985).

Archived upper air data were collected from radiosonde stations located within 200 km of the six volcanoes studied: Montserrat (Le Raizet, WMO 78897; Juliana Airport, WMO 78866); Mt. Augustine (King Salmon, WMO 70350; Anchorage, WMO 70273; Yakutat, WMO 70361); Mt. Spurr/Crater Peak (same as Mt. Augustine); Popocatepetl (Mexico City, WMO 76679); Ruapehu (Paraparaumu, WMO 93417; Whenuapai, WMO 93112); and Rabaul (WMO 91517; WMO 94014). These data were obtained from the NCDC and are in the Forecast Systems Laboratory (FSL) radiosonde format (Schartz and Govett, 1992). Software available through FSL was used to access the database, produce a Skew-T plot, and calculate derived sounding parameters such as tropopause level, total precipitable water, wind profile, and mixing ratio.

CONCEPTUAL MODEL OF VOLCANO-ATMOSPHERE INTERACTION

Dry Eruption Model

An eruption column (Fig. 1) consists of three components: the lowermost gas-thrust region; a convective-thrust region; and the uppermost umbrella region (Wilson, 1976; Sparks, 1986, Woods, 1988), as defined by both the velocity fields and the physical manifestations within each zone. This three-layer system applies to all volcanic columns, from those that are steady state systems supplied by a maintained release of materials from the vent to those that are produced by an instantaneous eruption and rise as an isolated thermal (Self and Walker, 1994).

The gas-thrust region attains a maximum height of about 3–5 km above the vent and has ascent velocities typically between 100 m s^{-1} and 500 m s^{-1} (Wilson, 1976; Sparks and Wilson, 1976). Some very violent eruptions, however, can exhibit vent velocities of 650–700 ms^{-1}, which is near the maximum possible under terrestrial atmospheric conditions (Self and Walker, 1994). This zone, where the eruption column can be characterized as a "jet" (i.e., flowing under very high positive pressure), is the gas thrust region. The temperature at the top of the vent (base of gas thrust region) is typically 600–1000°C (Sparks, 1986).

The convective-thrust region has a typical maximum height of 12–14 km (Turner, 1979). The typical range of ascent velocity within this region is 50–200 m s^{-1} (Sparks, 1986). The ratio of the height of the convective-thrust region above the vent, D_Z (Fig. 1), to the column radius at this height, D_B, is approximately constant with a value of 0.25 (Turner, 1979). Radial inflow velocities are about one-tenth of ascent velocities, so that radial inflow speeds of 5–20 m s^{-1} are typical (Turner, 1979). Extreme events for the most common types of eruptions (vulcanian, plinian) have ascent and radial inflow velocities corresponding to the extremes of the ranges cited above. Plumes associated with extreme events can reach altitudes as high as 30–35 km (Self and Walker, 1994). The convective-thrust region is defined as the zone of the eruption column in which vigorous turbulent forced-convection dominates, and accounts for 50–90% of the altitude attained by the eruption column (Self and Walker, 1994).

The umbrella region corresponds to the uppermost part of the convective rising region where the ascent velocities decrease and the slowing top of the column acts as a cap on the column (Self and Walker, 1994). Based on temperatures of the tops of eruptive columns (measured by thermal infrared sensors on NOAA weather satellites), the top of the umbrella is in marked thermal disequilibrium with the ambient temperature and may be undercooled by several tens of degrees Celsius. The undercooling is due in part to the extreme adiabatic expansion that occurs in the umbrella region (Self and Walker, 1994). The rising volcanic particle content, along with the lower temperature, produces a denser cloud than its surroundings. Thus, it tends to subside until it reaches a level of neutral buoyancy where the density of the volcanic cloud is nearly hydrostatically stable. The height of the neutral buoyancy layer, H_B, is approximately 0.7 times the total column height, H_T (Turner, 1979). The umbrella region of the eruption column is defined as the zone in which the plume deaccelerates and buoyancy is dissipated.

Wet Eruption Model

The dry eruption model works well when the gases involved were originally dissolved in the magma (Wilson, 1994). Three circumstances, however, can produce a wet adiabat: 1) radial entrainment of moist air into the column; 2) phreatic eruptions that are essentially steam-driven, as a result of contact between magma and ground water or ground ice; and 3) phreatomagmatic eruptions that occur when interaction between external water and magma produce explosive ejections of magmatic products, driven by both external and exsolving magmatic volatiles (Cas and Wright, 1987). All three conditions produce wet adiabatic as opposed to dry adiabatic rising conditions. Available eruption-column models, developed for dry eruptions, break down at some stage in the wet eruptions, but the relative proportions of magma to water and the magma volume and output rates at which the breakdown occurs are unknown (Wilson, 1994).

Nevertheless, recent significant work by Glaze et al. (1997) does indicate, from a theoretical standpoint, that entrained atmospheric water, surface, and/or magmatic water should substantially alter the development of the eruption column. In addition, they provide a paradigm for injection of substantial amounts of water (e.g., 4×10^9 kg H_2O_{vap} per hour for a ~20 km high plume) into the stratosphere from large explosive eruptions.

Radial Entrainment of Moist Air Masses

The standard display used by meteorologists to analyze the radiosonde vertical data is the Skew-T diagram (see the Appendix for a detailed discussion of the Skew-T diagram). Temperature, dewpoint, and winds are not plotted vertically but are angled off to the right at a 45° angle. Included on the Skew-T plot are levels for dry and saturation adiabats. Parcels of unsaturated air tend to follow the dry adiabat lines as they ascend or descend. Parcels saturated with water vapor will ascend the saturation adiabats. Descending parcels will tend to unsaturate immediately. Mixing ratio lines relate to the amount of water vapor in a parcel (g/kg of dry air). Parcels of air attempt to maintain a constant mixing ratio as they ascend or descend. A parcel will rise following the dry adiabat until it saturates. This occurs when the dry adiabat crosses the initial mixing ratio line. As lifting continues, the parcel cools following the saturation adiabat. By comparing the parcel temperature to the ambient temperature, one can determine whether the parcel is stable (cooler) or unstable (warmer). The unstable parcel will continue to rise until it reaches its hydrostatic equilibrium.

A Skew-T diagram of radiosonde data from King Salmon, Alaska, on 29 November 1998, and from Le Raizet, Guadeloupe near Montserrat on 16 November 1998, is shown in Figure 2. Two quantities of particular relevance to this work are the total precipitable water and the lifting condensation level. Total precipitable water (TPW) is the amount of water produced when all the water vapor in a column of air with unit cross-sectional area from the surface to the tropopause condenses. The lifting condensation level (LCL) is the level at which an initially unsaturated parcel of air becomes saturated through adiabatic expansion (Haltner and Martin, 1957). Typical values of TPW range from about 1.7 in. (40 mm)

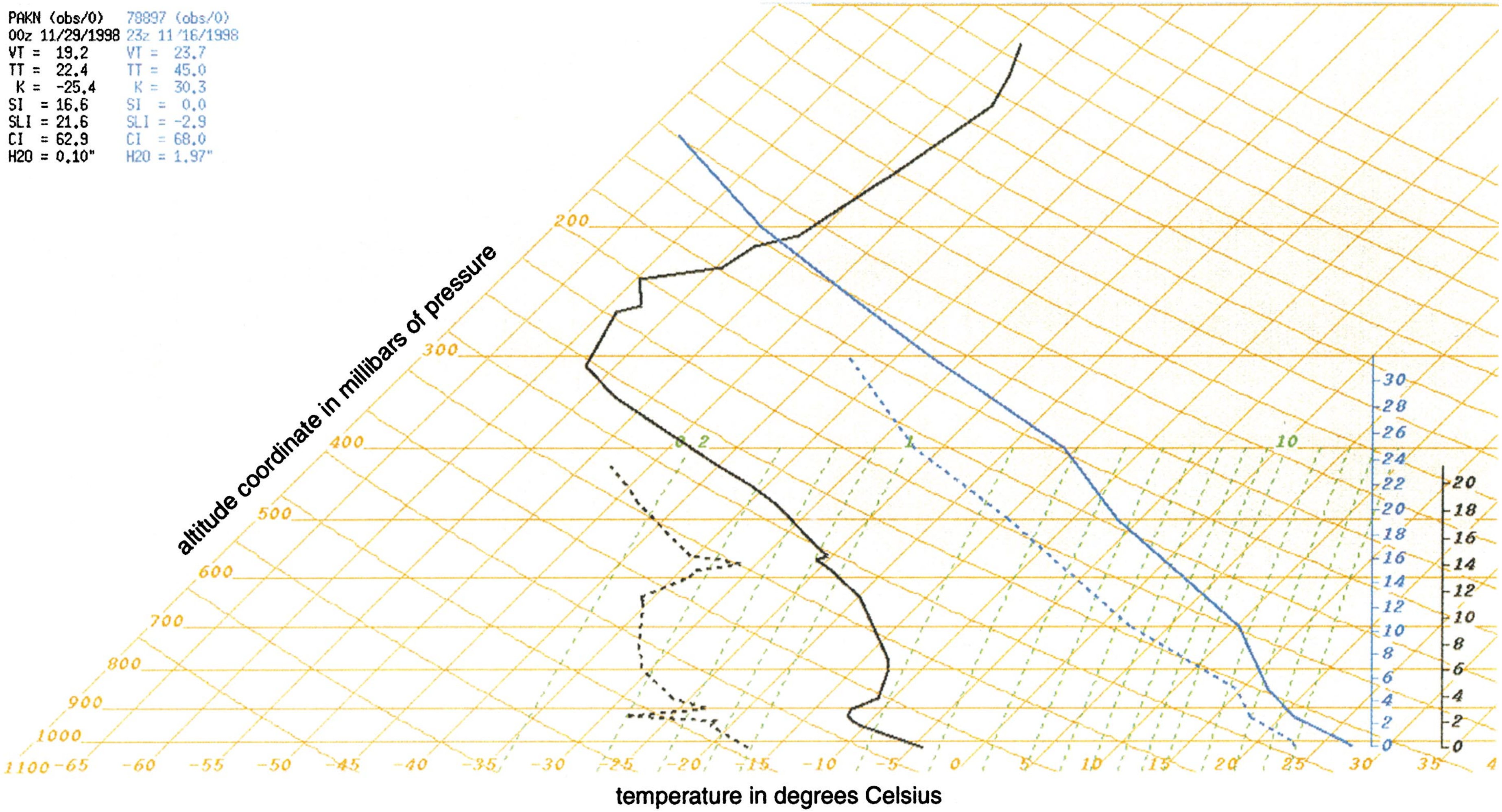

Figure 2. A Skew-T diagram of the radiosonde data (solid line is temperature, dashed line is wet bulb temperature) for King Salmon, Alaska (black traces) taken on 29 November 1998 and for Le Raizet, Guadeloupe (blue traces) taken on 16 November 1998.

in the tropics to about 0.2 in. (5 mm) at the poles (Moran and Morgan, 1997). The King Salmon, Alaska, and the Le Raizet near Montserrat data (Fig. 2) have lower and higher TPW, respectively, than these typical polar and tropical values. For a complete description of computed parameters, see Federal Meteorological Handbook FMH-3 (NOAA, 1981).

When an unsaturated parcel is lifted, it expands and cools at a dry adiabatic lapse rate of 10°C/1000 m. Once the parcel saturates, the moist parcel will then rise at a variable rate depending on the parcel temperature because warm saturated air releases more latent heat of condensation than cool saturated air. The greater the quantity of latent heat released the more the expansional cooling is offset. The moist adiabatic lapse rate ranges from 4°C/1000 m for very warm saturated air to almost 9°C/1000 m for cold saturated air. As long as the parcel continues to ascend, its temperature will drop.

In the volcanic eruption where large amounts of water may be entrained into the eruption column, the parcel will be supersaturated at very high temperatures. In a wet eruption, the parcel might slow as it rises at the moist adiabatic lapse rate. The parcel, however, continues to cool and remains supersaturated as it ascends, thereby increasing the moist adiabatic lapse rate. The latent heat release will continue to add to the positive buoyancy of the parcel, allowing it to reach even greater heights. As lead portions of the convective eruption column surge through the cloud top, they evaporate in the relatively drier ambient air above and thereby increase the water vapor pressure above the cloud. Because the air above the cloud is now more humid, subsequent portions of the eruptive cloud are able to ascend even higher. As this process is repeated, the cloud billows upward. The scenario presented here for the large heights obtained by wet eruptive columns is very similar to the process that leads to the high vertical heights of thunderstorm cumulus clouds. Ultimately, what sets the height limit on the eruptive cloud is the balance between the gravitational pull on the volcanic ash load and the buoyancy in the cloud.

Surface Water, Snow, Ice and Ground Water

When molten rock comes into contact with ground water, surface water from lakes, marshes, littoral areas or rivers, snow or ice, a hydrovolcanic eruption occurs. The formation and collapse of stream films at the water/molten rock interface causes deformation and fragmentation of the melt and explosive expansion of high-pressure steam (Heiken, 1994). The rapid superheating of water results in eruptions that 1) are more efficient at fragmenting and dispensing volcanic ash than those that are driven by bubble growth and decompression alone and 2) can have very high water vapor content in the eruptive column and thus enhance the wet adiabatic effects on plume height, ascent, and radial inflow velocities described above. Hydrovolcanic ashes generally have very fine grains (median grain size can be as small as 40 μm). Very fine grain size particles (<10 μm), which can be produced by this type of eruption, can stay in the stratosphere long enough to be transported thousands of kilometers from the vent (Self and Sparks, 1978; Wilson, 1994). Hereafter, the term surface and ground water refers to solid (snow, ice) as well as liquid water.

Juvenile Water

Dissolved magmatic volatiles can strongly affect the character of explosive eruptions. The dominant magmatic volatile in nearly all terrestrial magmas is water, followed by carbon dioxide. Confining pressure is a major factor controlling the solubility of dissolved volatiles. As magma ascends through the crust, decreased confining pressures allow the exsolution of these dissolved volatiles into separate fluid and/or vapor phases. As magma nears the surface, the exolved fluid and vapor phases will add to the pressurization of the eruption conduit and magma chamber, and enhance the explosive character of the eruption. This is particularly true if additional surface and near-surface free water is encountered in the course of magma ascent, and a phreatomagmatic eruption results.

At constant temperatures, the solubilities of water in basalt, andesite, and rhyolite are not significantly different. For instance, at 1000 kb and 1100°C, basalt (45–52% SiO_2) has an average H_2O solubility of about 2.5% versus 4.5% for andesite (57–63% SiO_2) (Williams and McBirney, 1979; Cas and Wright, 1987). Higher silicate magmas, however, typically have larger water solubilities because they erupt at lower temperatures (Hamilton, et al., 1964). Basalts typically have less water than rhyolites because their eruption temperatures are significantly higher (i.e., ~1100°C for basalt versus ~800°C for rhyolite).

RESULTS

Six eruptions were analyzed as part of this study. For each eruption, radiosonde data in close proximity to the volcano were obtained to characterize the atmosphere. Likewise, various sources of geologic data were obtained to characterize the volcano, the specific eruption under study, and provide a basis for estimating juvenile water and surface and ground water. UTC times are used throughout. Each eruption is discussed separately below. With the exception of Popocatepetl (~7km ASL), the eruptions studied here all projected eruption plumes to altitudes between 10 km and 15 km, corresponding to eruption rates at the vent of roughly 10^3 m^3/s (Woods, 1988). This volumetric eruption rate and umbrella cloud altitude roughly correspond to the minimum size eruption of relevance to transoceanic and transcontinental aircraft, because most aircraft on those routes cruise at altitudes equal to or greater than 10 km (~32K ft). Such eruptions are fairly typical of many volcanoes worldwide. Any difficulties arising with the $T_4 - T_5$ technique for detecting this class of eruption would thus be particularly disturbing.

For plots of T_4-T_5 versus T_4 only pixels in the actual plume of a given image were considered. These pixels were identified manually by creating a small search area that encompassed the plume. Generally, plume pixels have a temperature less than a threshold *T*, whereas surrounding ocean or land pixels have higher temperatures. The value of *T*, however, is not constant from scene to scene for a given eruption and must be determined manually by trial and error. Moreover, for some plumes this method is not totally successful. Under these circumstances, the operator must visually move the computer mouse to trace out the locus of plume pixels. In principle, this procedure should provide the best test population of pixels which satisfy the negative T_4-T_5 volcanic ash plume detection criterion.

Soufriere Hills (Montserrat)

The Soufriere Hills volcano is located in the tropical Caribbean Sea (16.72°N; 62.18°W). The vent is 0.915 km above sea level (ASL). An eruption occurred on 18 September 1996. The average height of ash cloud was 13 km ASL (Robertson et al., 1998). The troposphere height was 14.4 km, the mean total precipitable water vapor was 1.89 ± 0.20 in. and the mean lifting condensation level was 1.16 ± 0.07 km as determined from radiosonde data.

Low end estimates of juvenile water in the magma vary between 2.04×10^5 m^3 to 2.80×10^5 m^3 based on geochemical and petrological analysis of undergassed clasts. High end estimates of juvenile water vary between 3.39×10^5 m^3 to 4.24×10^5 m^3 based on eruption dynamics. Estimates of surface and ground water are taken as 2×10^4 m^3 to 40×10^4 m^3, assuming it varies between 1% and 10% of juvenile water. Observations of the initial eruptions of the Montserrat series (e.g., 1995) noted phreatomagmatic activity as well as standing water in the craters. This may have indicated some degree of saturation of the pre-1997 eruption summit deposits by accumulated meteoric water. Also, the presence of hot springs indicated an established hydrogeothermal circulation system. By 1997, however, such surface water was probably "baked out" because this eruption is described by Robertson et al. (1998) as "magmatic" as opposed to phreatomagmatic (also see Young et al., 1998).

Panels a–h of Figure 3 show a time series of GOES-8 data (T_4). The first element in the time series was taken 3 min after the eruption. Because of a data capture error, the second element in the time series is about 3 h later. The remaining six elements in the time series occur at hourly intervals after the time of the second element. The volcanic plume is clearly visible in panels b, c, and d of Figure 3 (see area in blue box). As time progresses, the plume signature in the satellite data begins to dissipate (Fig. 3, panels e, f, g, and h). Panels i–p of Figure 3 are analogous panels a–h of Figure 3, except results obtained with the T_4-T_5 detection algorithm are shown. Negative values of T_4-T_5 imply volcanic ash (green overlay). The T_4-T_5 volcanic ash detector failed to correctly classify the vast majority of pixels in the volcanic ash plume as volcanic ash plume pixels. Moreover, it consistently mislabeled meteorological clouds in the scenes, often geographically far removed from the actual volcanic plume, as volcanic ash plume pixels.

Figure 4 shows plots of T_4-T_5 versus T_4 for data only within the actual plume. Panels a–g in Figure 4 correspond to panels b–h and j–p in Figure 3. Pixels within the volcanic plume, which the T_4-T_5 detection algorithm incorrectly interpreted as meteorological clouds (positive T_4-T_5 values), appear as blue X's in these panels. Pixels which the T_4-T_5 detection algorithm correctly interpreted as volcanic ash plume pixels (negative T_4-T_5 values), appear as red X's. The number of pixels in the plume, the percent of false detections (positive T_4-T_5 values) and the percent of true detections (negative T_4-T_5 values) are given for each time step in the series above that time step's panel. False classification rates vary between 95% and 99%.

Mt. Spurr/Crater Peak

The Mt. Spurr/Crater Peak volcano is located in Alaska (61.30°N; 152.25°W). The vent is 2.309 km ASL. An eruption occurred on 19 August 1992. On 19 August at 1458 UTC the height of the ash cloud was 11 km ASL. Radar observations of ash at 1455 UTC, however, reported a height of 13.7 km (Rose et al., 1995). Radiosonde data for this eruption gave a tropopause height between 9.1 km and 11.6 km, total precipitable water between 0.25 in. and 0.6 in. and a lifting condensation level between 0.79 km and 3.04 km. Clearly, total precipitable water for the Mt. Spurr/Crater Peak eruption is considerably less than for the Soufriere Hills (Montserrat) eruption, consistent with the drier characteristics of the polar atmosphere.

Large SO_2 emissions were possible during the three explosive eruptions because the magma ascended rapidly to the surface and could degas directly into the atmosphere. This effectively prevented contact with liquid water and loss by scrubbing of most of the SO_2 released during the eruptions. Therefore, estimated juvenile water, based on the estimated saturation percentage for an andesitic magma chamber at 2 km depth and 1100 °C (Fisher and Schmincke, 1984), is taken as 9.29×10^5 m^3. TOMS data for this eruption also indicate that 15–20% of the sulfur released in the three eruptions was emitted as H_2S (Bluth et al., 1995). This suggests that H_2S emissions might also have occurred from the boiling of water during the explosive events (Doukas and Gerlach, 1995). Under these circumstances, aqueous SO_2 is thermody-

Montserrat Eruption Sequence (September 18, 1996)

Eruption Began at 03:42 GMT on 9-18-96 (All images are in GMT time)

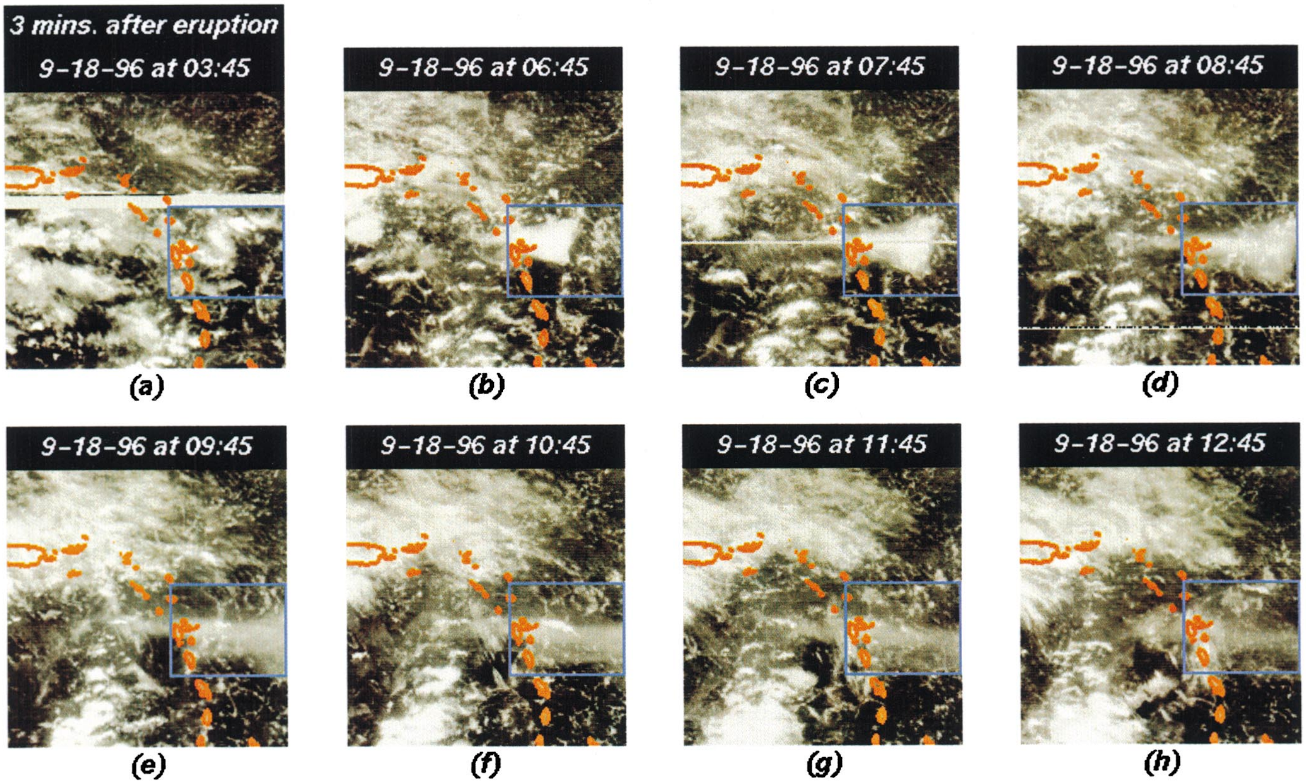

Volcanic Ash Detected by the T_4 - T_5 Subtraction Algorithm (e.g., Schneider and Rose, (1995))

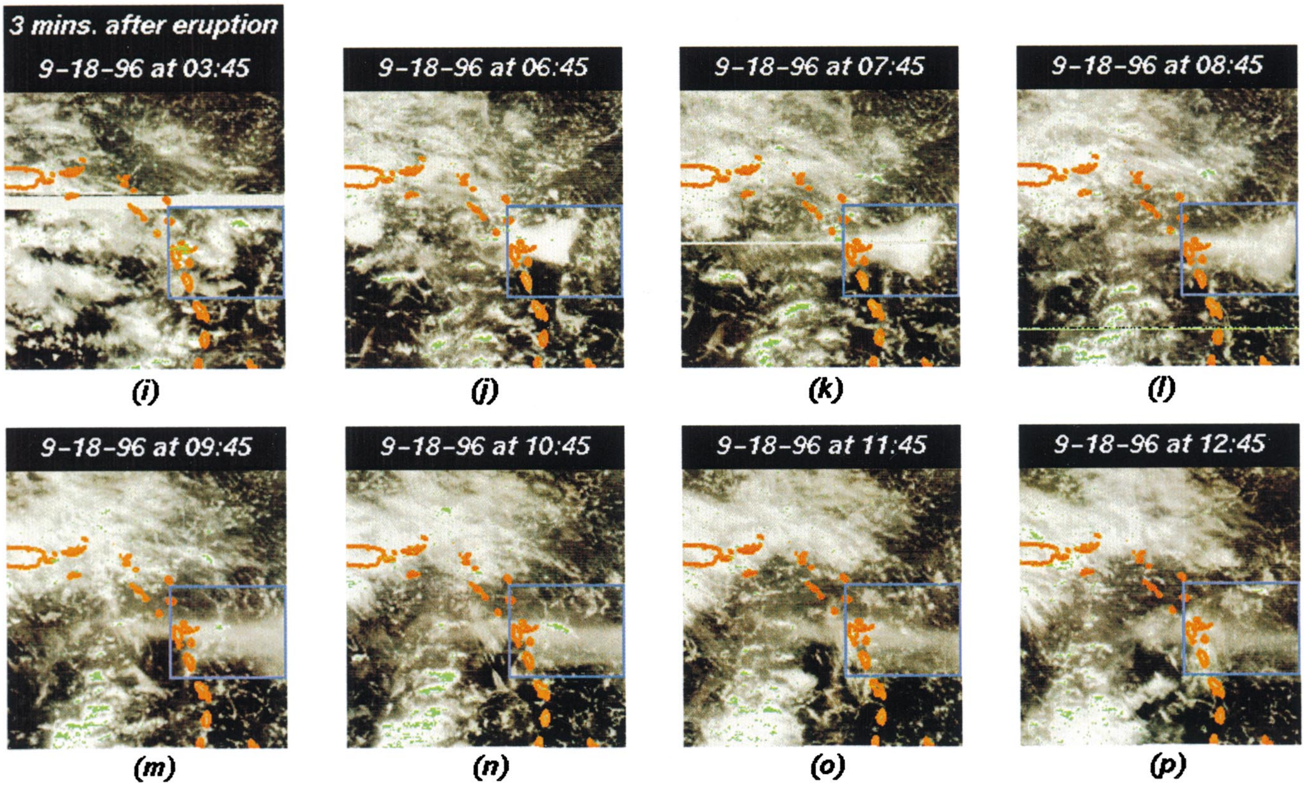

Figure 3. Panels a–h present a time series of GOES-8 (T_4) for the Montserrat eruption with GMT data/time given. The blue box surrounds the eruption plume in a given scene; the coastline is orange. Pixels detected as volcanic ash plume pixels by the T_4-T_5 algorithm appear as the green overlay in panels i–p. Volcanic ash should have negative T_4-T_5 values if a reverse absorption effect is the dominant process affecting the T_4 and T_5 brightness temperature retrievals. The T_4-T_5 algorithm grossly underdetects volcanic ash in the plume and misinterprets meteorological clouds as volcanic plume.

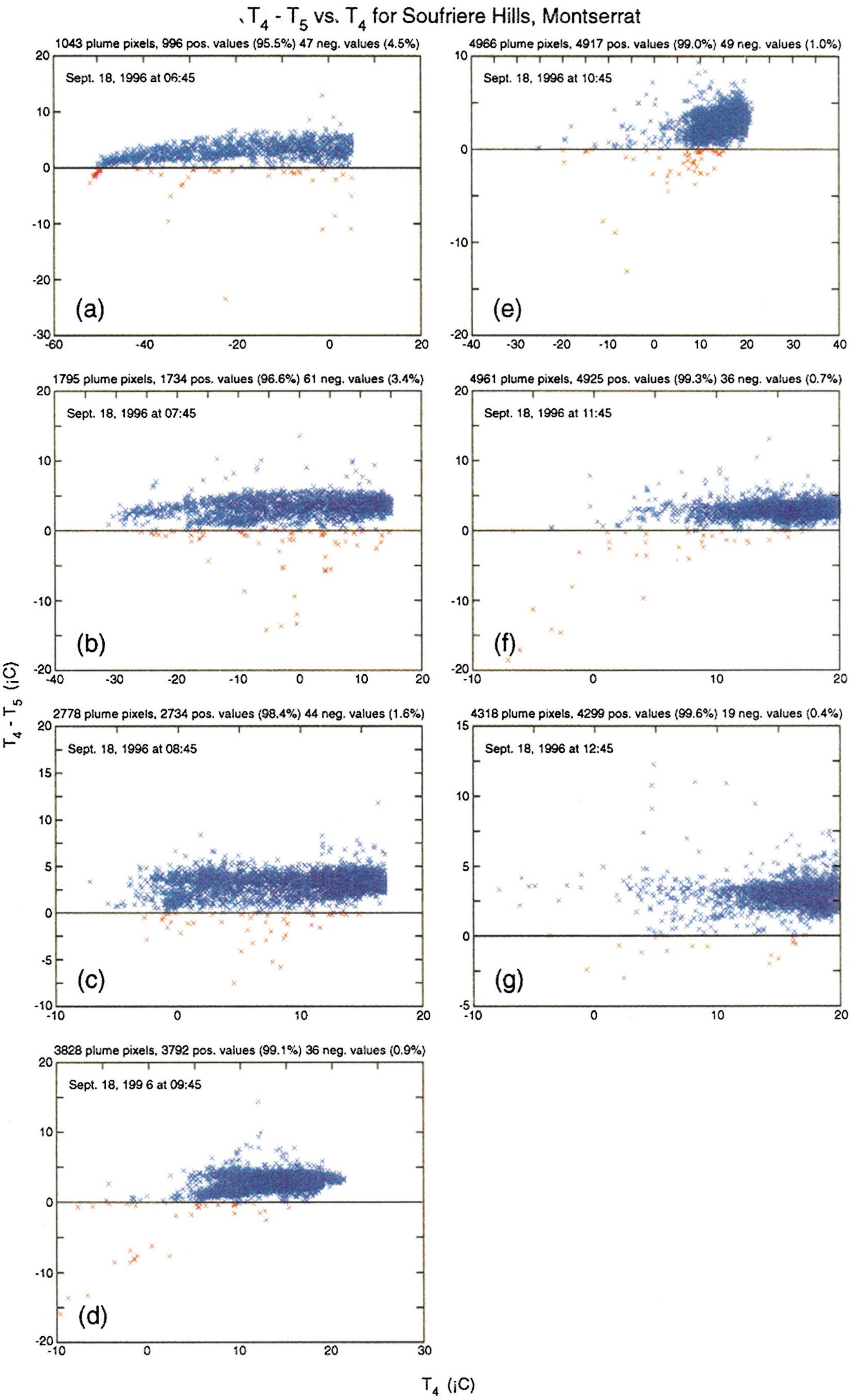

Figure 4. Plots of T_4-T_5 versus T_4 for pixels in the Montserrat volcanic ash plume only. Panels a–g correspond to panels b–h and panels j–p in Figure 3. Blue X's (positive T_4-T_5) indicate incorrect assignment of pixels in the volcanic ash plume to the meteorological cloud class. Red X's (negative T_4-T_5) indicate correct classification as volcanic plume pixels.

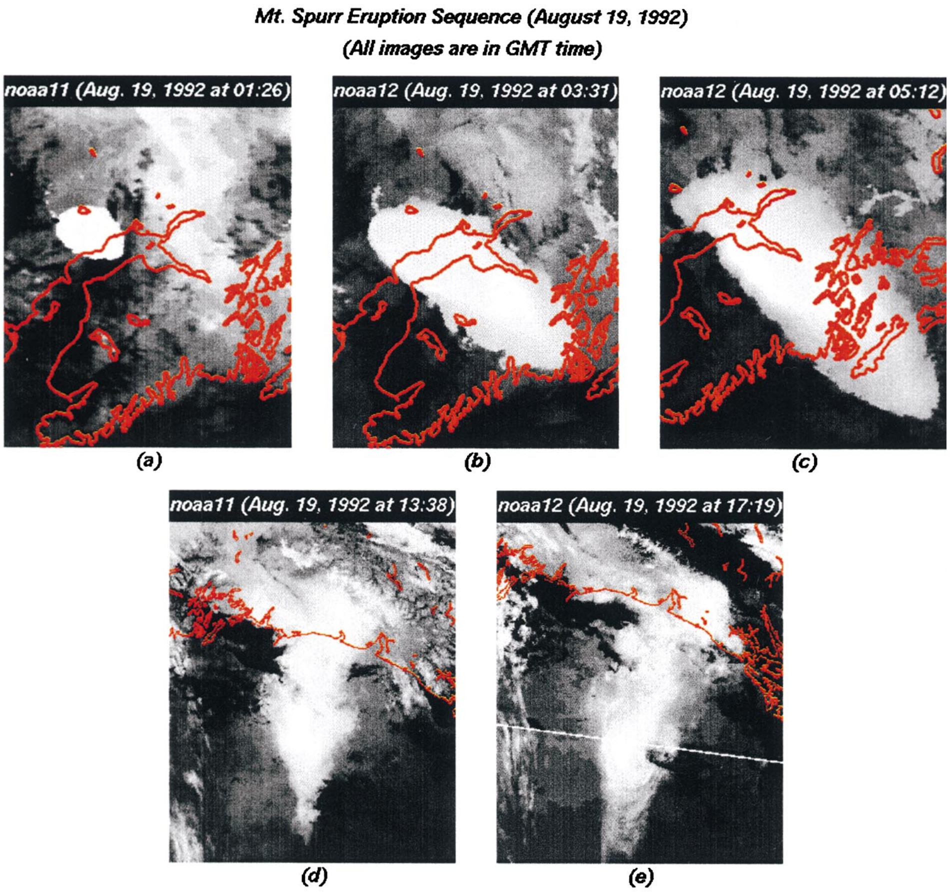

Volcanic Ash Detected by the T_4 - T_5 Subtraction Algorithm (e.g., Schneider and Rose, (1995))

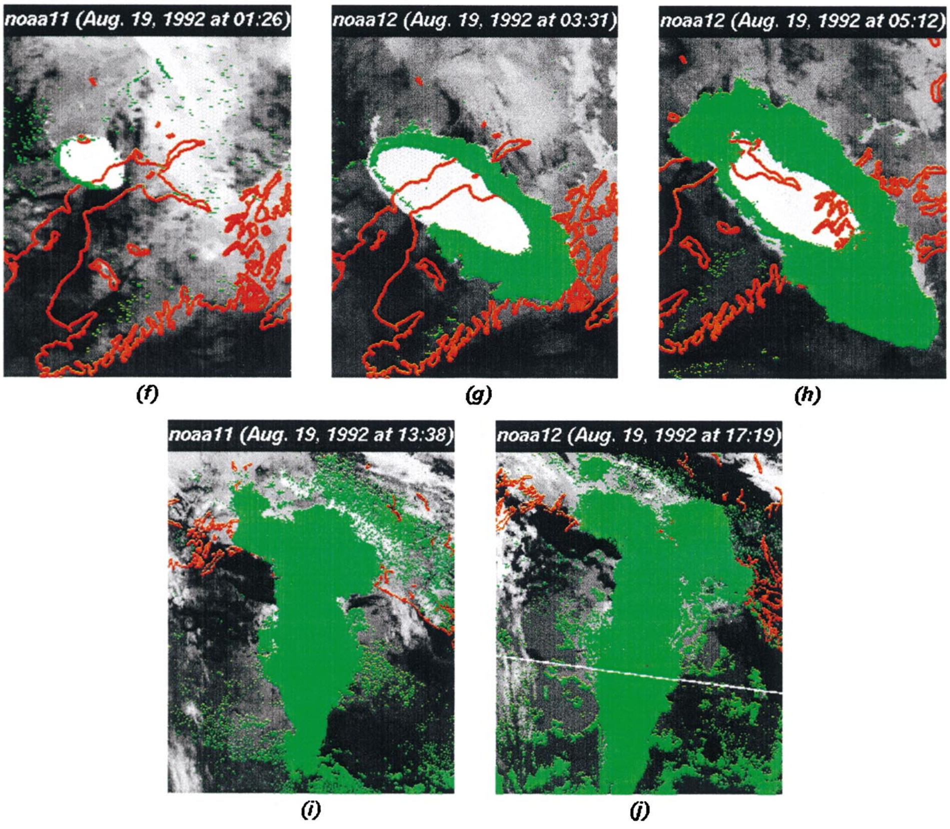

Figure 5. Panels a–e present a time series of AVHRR T_4 data for the Mt. Spurr/Crater Peak, Alaska eruption with GMT data/time. Pixels detected as volcanic ash plume pixels by the T_4-T_5 algorithm appear green and coastlines appear orange in panels f–j. The T_4-T_5 grossly underdetects volcanic ash up to 4 h after the eruption (panels f, g), still has a significant failure rate 6 h after the eruption (panel h), and falsely classifies large amounts of meteorological cloud as volcanic ash during the later stages of the eruption (panels i, j).

namically unstable in water relative to sulfate species and aqueous H_2S, except at temperatures greater than 300 °C and for pH values ≤ 2. The hydrolysis of SO_2 by the disproportionation reaction [Eq. (1)],

$$4H_2O\ (1) + 4SO_2\ (aq) \rightarrow H_2S\ (aq) + 3H_2SO_4\ (aq), \quad (1)$$

proceeds strongly in the direction indicated. Because magmas generally emit more SO_2 than H_2S, the production of H_2S by hydrolysis was probably significantly greater than its generation from magmatic degassing. Therefore, the estimate of ground water is based on a calculation of the equivalent amount of water necessary to produce the 75 kT H_2S that Bluth et al. (1995) assumed was required to produce the SO_2 pattern observed in their TOMS data. This procedure yields an estimate of ground water between 1.11×10^5 m^3 and 2.06×10^5 m^3.

Panels a–e of Figure 5 show a time series of AVHRR T_4 data, taken on 19 August 1992, from both NOAA-11 and NOAA-12 to get high temporal resolution for the event. The first three elements are about 2 h apart in time and capture the early stages of the eruption. The last two elements occur many hours after the eruption and show final stages of plume development and dispersion. Panels f–j of Figure 5 are analogous to panels a–e of Figure 5, except results obtained with the T_4-T_5 volcanic ash detection algorithm are shown. Negative T_4-T_5 values imply volcanic ash (green overlay) and coastlines appear orange. Again, these data show that the T_4-T_5 volcanic ash detector failed to accurately classify the vast majority of volcanic ash plume pixels in the early stages of the event (Figs. 5f and 5g). Even 6 h after the event, the central core of the ash cloud was not detected, and significant parts of the volcanic cloud edge were not properly classified (Fig. 5h). During the later stages of the eruptions (Figs. 5i and 5j), the T_4-T_5 procedure successfully classified almost all the pixels in the volcanic ash cloud correctly. Unfortunately, large amounts of meteorological cloud also were incorrectly classified as volcanic ash cloud.

Figure 6 is analogous to Figure 4, except AVHRR data are used instead of GOES-8 data and there is a direct one to one correspondence between Figure 5, panels a–e, Figure 5, panels f–j, and Figure 6, panels a–e. Again, data in Figure 6 correspond only to actual plume pixels. The percentage of plume pixels falsely classified as meteorological clouds is 89.3%, 51%, and 28.3% in AVHRR data taken about 2 h, 4 h, and 6 h after the eruption, respectively.

Mt. Augustine

The Mt. Augustine volcano is located in Alaska (59.37°N; 153.42°W). The vent is 1.282 km ASL. A series of eruptions occurred from 28 to 31 March 1986. The height of the volcanic plume varied from 6.1 km ASL to 6.7 km ASL on 28 March 1986 and from 11.6 Km ASL to 12.2 km ASL at 1852 UTC on 31 March 1986. Young et al. (1987) gave an estimate of greater than 12 km ASL for the plume height. Radiosonde data showed that the atmosphere for the Mt. Augustine area was extremely dry. Total precipitable water vapor varied between 0.08 in. and 0.2 in. The mean tropospheric height was 11.3 km with a standard deviation of 2.1 km. The mean lifting condensation level was 1.7 km with a standard deviation of ±0.09 km.

Juvenile water is estimated to be 2.43×10^6 m^3 based on saturation pressure for a 2 km deep magma chamber. The volume of the eruption is assumed comparable to the volume of the large pyroclastic flow. Eruption density used is one-third of the dense rock equivalent. The estimate of surface ground water is based on the known areal extent of snow cover at the summit, 2–3 km^2. A maximum snow depth of 10 m over this surface area was assumed. As a zero-order approximation, the total ground water involved was assumed about one-tenth the volume of snow.

Panels a–d of Figure 7 are analogous to panels a–e of Figure 5, except the AVHRR data are from NOAA-9. A Lambert equal area projection was used; coastlines are orange. The blue boxes in these panels highlight the volcano and eruption plume. There was little evidence of an eruptive event in the third element of the sequence (panel c). Major changes in wind direction also occurred during the sequence of eruptions as indicated by the changes in direction of the volcanic ash plume dispersal. Panels e–h of Figure 7 are analogous to panels a–d of Figure 7, except pixels detected as volcanic ash plume by the T_4-T_5 detection algorithm appear as the green overlay. Clearly, the T_4-T_5 algorithm falsely detects significant amounts of meteorological cloud as volcanic ash cloud. This is especially of concern for the data in panel f where large amounts of meteorological cloud near the volcanic plume are misclassified and imply that the areal extent of the volcanic ash cloud is much larger than it actually is (compare Figs. 7b and 7f).

Figure 8 is analogous to Figure 6, except for the Mt. Augustine eruption and panels a, b, and c in Figure 8, correspond to panels a, b, and d in Figure 7 and panels e, f, and h in Figure 7. Data for 29 March 1996 at 23:56 UTC were not used in this analysis (Fig. 7c) because the volcanic plume is not easily discernable in this particular image. Data in Figure 8 correspond only to actual plume pixels. The percentages of plume pixels falsely classified as meteorological cloud are 24.0%, 18.9%, and 8.19%, respectively. This higher success rate (compared to the other examples shown) is related to the relative dry winter arctic atmosphere as determined from the radiosonde data and the relative low amounts of juvenile water and surface and ground water compared to the other eruptions studied.

Ruapehu

The Ruapehu volcano is located on the North Island of New Zealand (39.28°S; 175.57°E). The vent is 2.779 km ASL. An eruption occurred on 16–17 June 1996. The average height of the ash cloud was between 8 km ASL and 10 km ASL.

Panels a–i of Figure 9 show a sequence of nine GMS-5 images with their respective UTC dates and times given in its corresponding panel and the New Zealand coastline shown in orange. The sequence spans about a half a day in time. The plume is easily seen in panels b–f as it expands northeast over time (see the sequence of expanding blue boxes in these panels). The plume becomes more difficult to see in panels h and i as it dissipates. Panels j–r of Figure 9 are analogous to panels a–i of Figure 9, except pixels detected as volcanic ash using the T_4-T_5 algorithm appear green. In the early stages of the eruption, the T_4-T_5 detection algorithm fails to completely detect the plume. Only several hours after the eruption, does the algorithm detect most of the plume structure. Again, some meteorological clouds were falsely assigned to the volcanic ash plume class.

Figure 10 is a plot of T_4-T_5 versus T_4 for this event; panels a–e correspond to panels b–f and k–o in Figure 9. Again, data in these plots are for plume pixels only. Percent misclassifications (volcanic plume pixels are assigned to the meteorological cloud class) are 58.3%, 41.0%, 25.6%, 26.9%, and 45.9% for the appropriate periods 2 h, 4 h, 6 h, 8 h, and 10 h after the eruption, respectively.

Popocatepetl

The eruption at Popocatepetl, Mexico (19.023°N; 98.622°W) occurred on 10–11 March 1996. The vent is 5.426 km ASL. The height of the ash cloud varied between 5.5 km and 7.0 km. Radiosonde data give a tropospheric height between 14.3 km and 14.9 km, total precipitable water is low varying between 0.16 in. and 0.56 in. and the lifting condensation level varies between 1.82 km and 3.70 km. Surface and ground water was estimated to be less than 1.7×10^4 m^3 and juvenile water estimates vary between 1.7×10^4 m^3 and 3.4×10^4 m^3.

Panels a–i of Figure 11 show a time series (1.5 h time step) of GOES-8 T_4 data over Mexico (coastline orange) for the 10–11 March 1996 eruption. The UTC time for each image is also given in Figure 11, panels a–i. The blue boxes in panels a–e enclose the volcanic plume. Panels j–r of Figure 11 are analogous to panels a–i of Figure 11, except pixels detected as volcanic plume pixels by the T_4-T_5 detection algorithm appear green. Large false detection of meteorological cloud as volcanic ash cloud occurs.

Figure 12 shows plots of T_4-T_5 versus T_4 for the Popocatepetl eruption at selected time steps. Data points are for the pixels within the volcanic plume only. Initially, the false detection rate is about 36.1% (panel a). Throughout the remainder of the eruption the failure rate varies between about 22% and about 37%.

Rabaul

The eruption at Rabaul, Papua New Guinea (4.27°S, 152.2°E) occurred on 19–20 September 1994. The vent is 0.688 km ASL. The height of the ash cloud varied between about 1.1 km ASL and 1.7 km ASL. Surface and ground water was estimated to be $<1.7\times10^4$ m^3. Juvenile water estimates varied between 1.7×10^4 m^3 and 3.4×10^4 m^3. Satellite and radiosonde data for the eruption period are limited.

Panels a–c of Figure 13 show plots of T_4-T_5 versus T_4 for the Rabaul eruption at selected times. Data points are for pixels within the volcanic plume only. Initially, the false detection rate is 99.5%. Fourteen hours later the false detection is still very large, 97.9%. It improves only slightly to a false detection rate of 76.5% on 20 September 1994 at 7:20 UTC. Figure 13d shows the time line and areal extent of plume eruption as determined by the Global Volcanism Program of the National Museum of Natural History at the Smithsonian Institution. Figure 13d, compared with the other panels in Figure 13, indicates that the T_4-T_5 procedure performed very poorly for the Rabaul eruption. The reduced spatial resolution of the available GAC data, compared to full resolution Local Area Coverage (LAC) data, further compromised the results obtained from the T_4-T_5 algorithm.

DISCUSSION

Synthesis of Results

Satellite data, which monitored six different volcanic eruptions, were analyzed. These eruptions have wide variations in ambient atmospheric water vapor, available ground and surface water, and different magma types associated with varying amounts of juvenile water. Figure 14a shows a plot of percent negative T_4-T_5 pixels in the Montserrat plume as a function of time. Most accurate detection in these plots corresponds to 100% negative T_4-T_5 pixels in the volcanic plume at a given time step. Best results for the Montserrat eruption were obtained about 3 h after the eruption, but only 4.5% of the total plume pixels were correctly classified. As time progressed, the classification accuracy decreased even further to only 0.45% about 9 h after the eruption. Figure 14b is analogous to Figure 14a, except for the Mount Spurr/Crater Peak

Figure 6. Plots of T_4-T_5 versus T_4 for pixels in the Mt. Spurr/Crater Peak volcanic plume only. Color codes are analogous to those of Figure 4.

Figure 8. Analogous to Figure 4, except for Mt. Augustine. Panels a, b, and c here correspond to panels a, b, d and e, f, h of Figure 7.

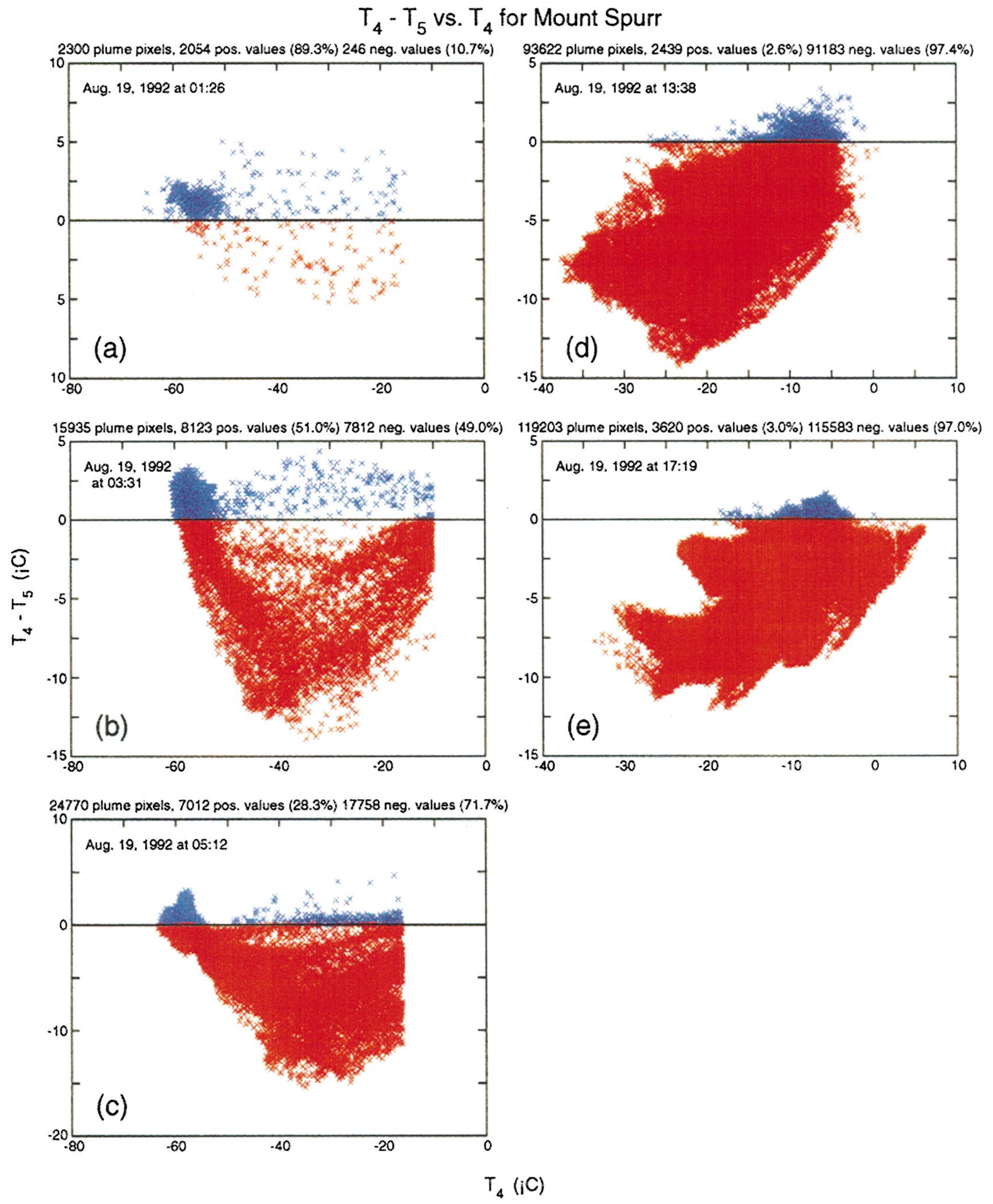

Figure 6.

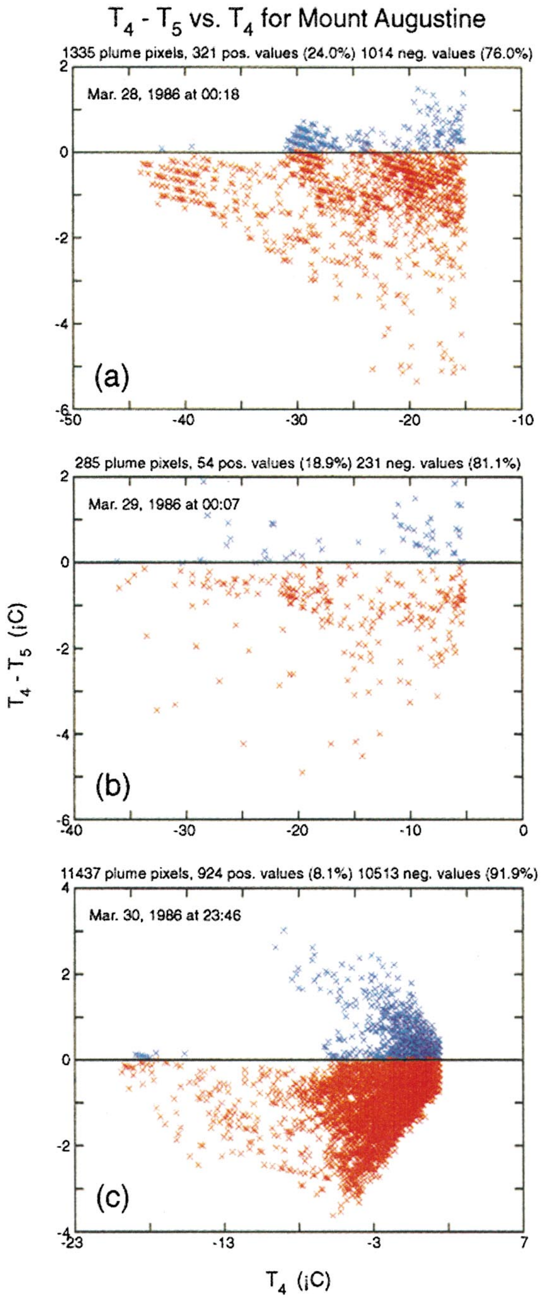

Figure 8.

Augustine Eruption Sequence (3-28-86 to 3-30-86)

(All images are in GMT time)

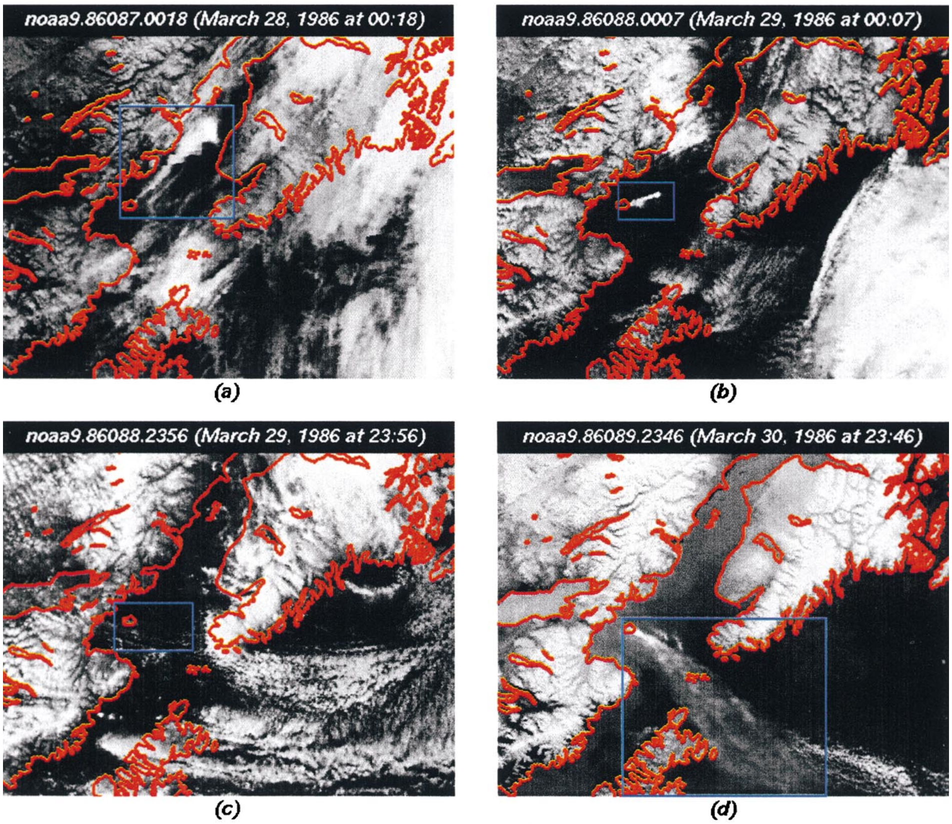

Volcanic Ash Detected by the $T_4 - T_5$ Subtraction Algorithm (e.g., Schneider and Rose, (1995))

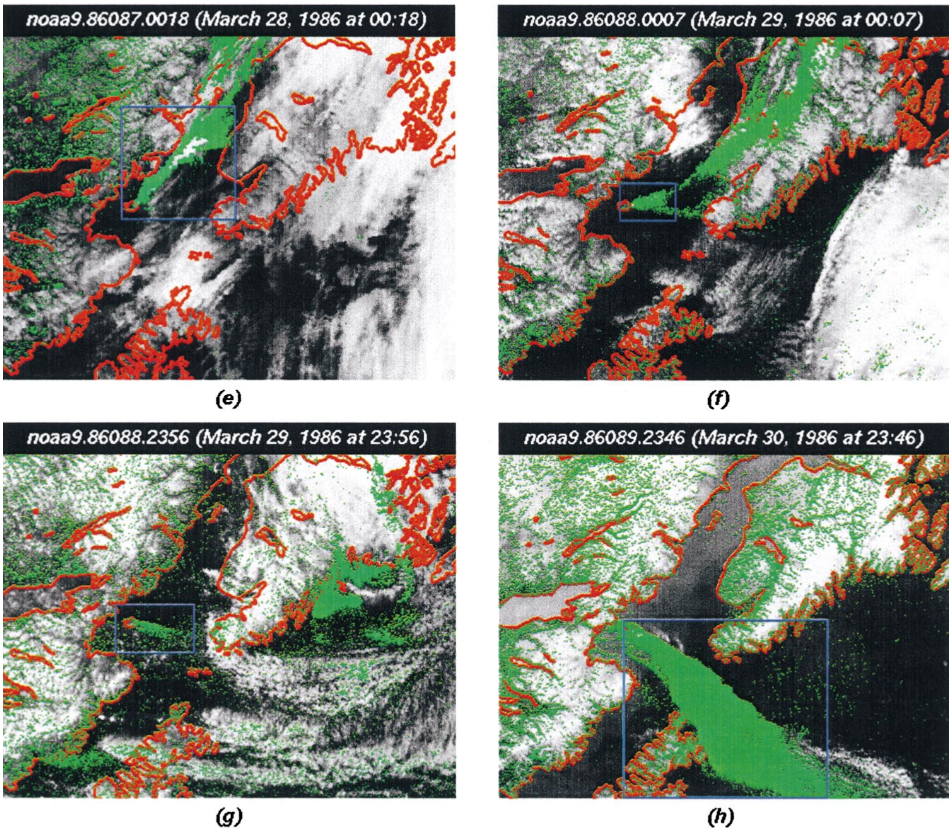

Figure 7. Panels a–d are analogous to panels a–e of Figure 5, except the AVHRR data are from NOAA 9 for Mt. Augustine. Panels e–h are analogous to panels f–j of Figure 5.

Ruapehu, New Zealand Eruption Sequence (June, 1996)
(All images are in GMT time)

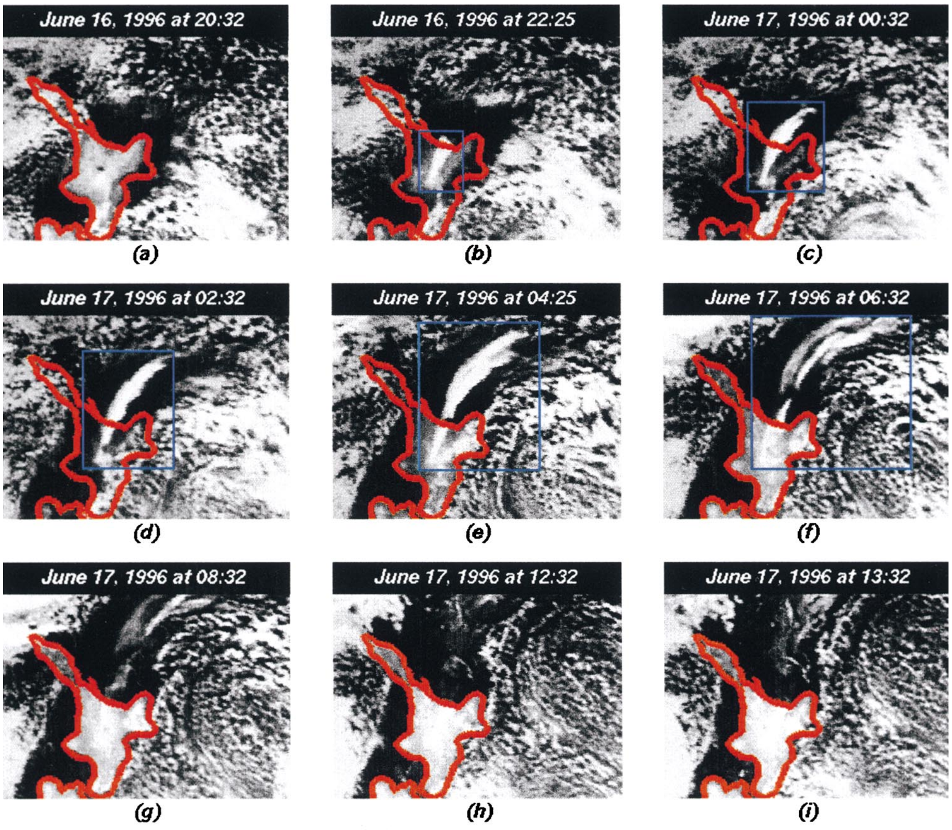

Volcanic Ash Detected by the $T_4 - T_5$ Subtraction Algorithm (e.g., Schneider and Rose, (1995))

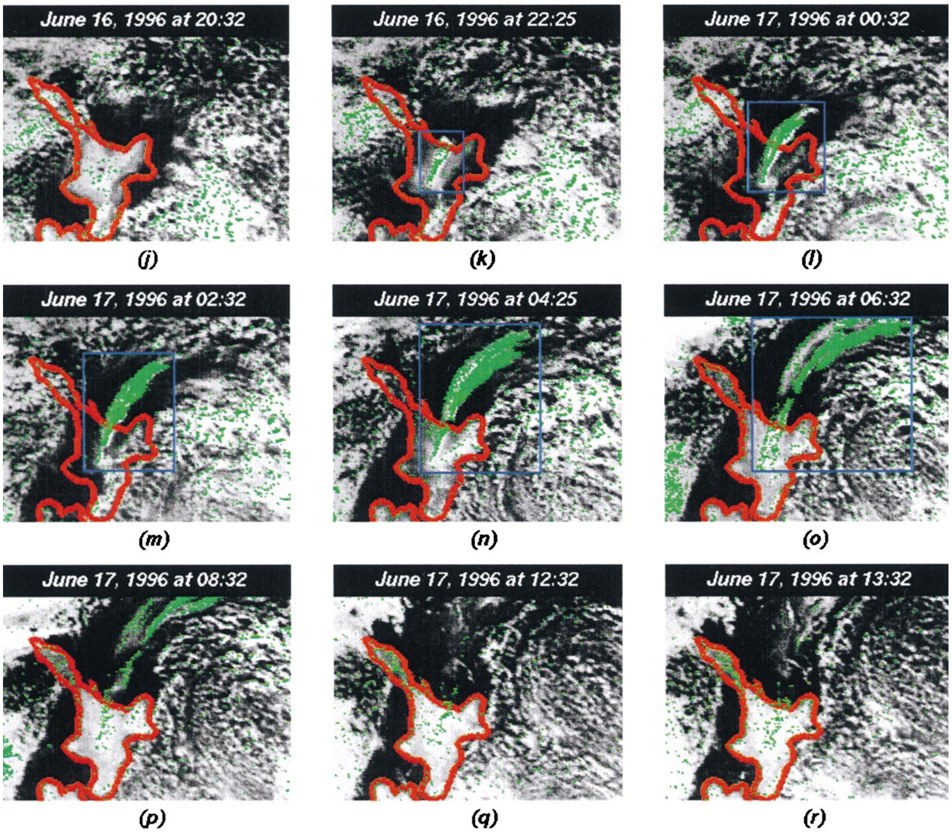

Figure 9. Panels a–i present a time series of nine GMS-5 T_4 images, with their respective GMT dates and times for the Ruapehu, New Zealand eruption 16–17 June 1996. Coastlines are orange. Areas of eruption activity are in the blue boxes. Pixels classified as volcanic ash plume pixels by the $T_4 - T_5$ detection algorithm appear green in panels j–r. Orange is coastline.

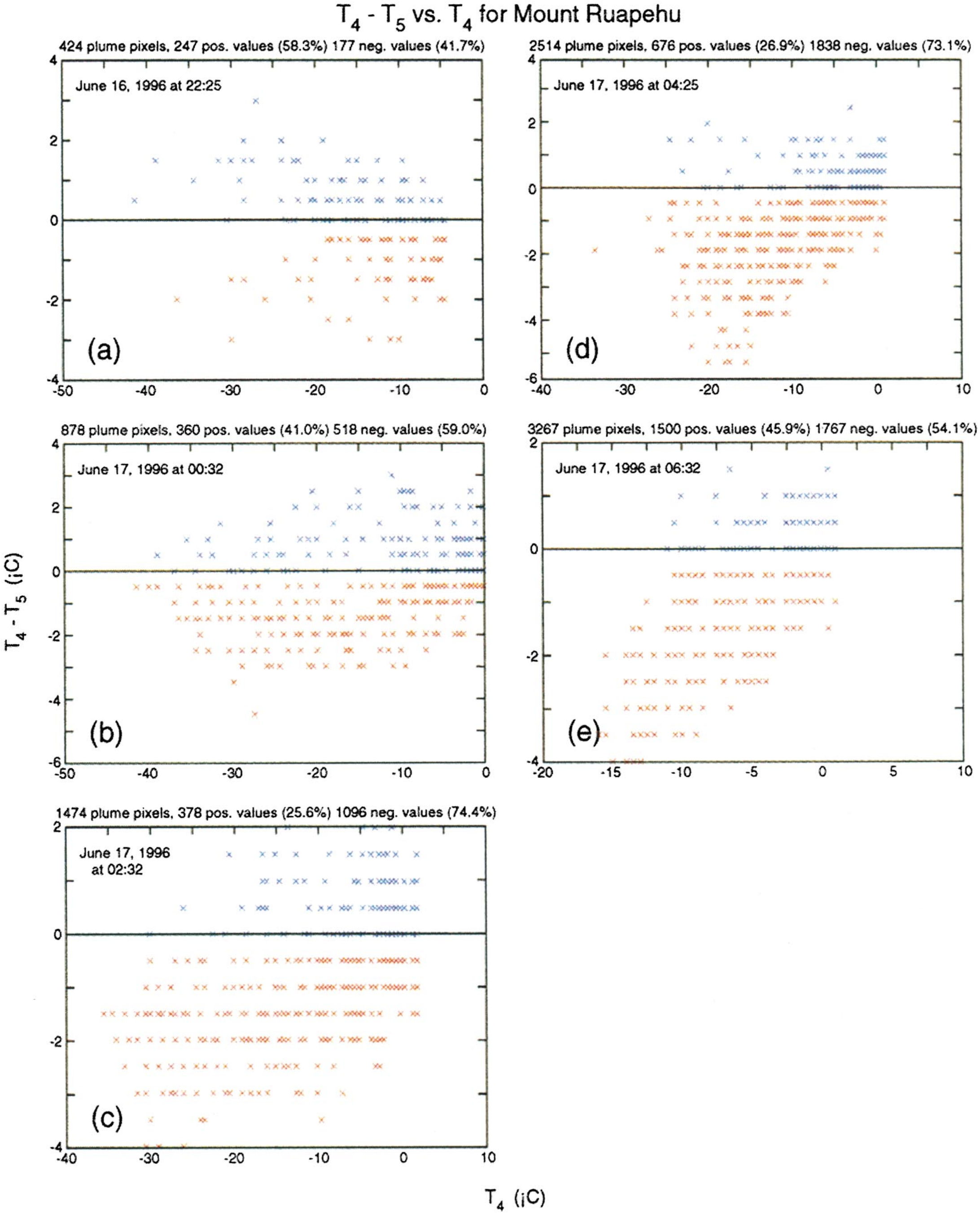

Figure 10. Analogous to Figure 4, except GMS-5 data for the Ruapehu eruption. Panels a-e here correspond to panels b–f and k–o of Figure 9.

eruption. Acceptable levels of plume detection only occur about 12–14 h after the eruption; a result inconsistent with aviation early warning needs. Figure 14c is analogous to Figure 14a, except for the Ruapehu, New Zealand, eruption. Clearly, the percent of true classification, as well as the time after the eruption for lowest error rate in classification, are unacceptable for aviation needs. Moreover, the predictive skill did not increase over time as with the Mt. Spurr/Crater Peak and the Mt. Augustine eruptions but rather again obtained a rather high failure rate towards the end of the sequence. Figure 14d is analogous to Figure 14a, except for the Popocatepetl eruption. The oscillatory behavior of these data shows that the T_4-T_5 algorithm never achieved acceptable classification skill.

The results show that the generally used T_4-T_5 test for volcanic ash pixels (negative T_4-T_5 values) is not uniformly effective in properly classifying volcanic ash pixels

Popocatepetl, Mexico Eruption Sequence (March, 1996)

(All images are in GMT time)

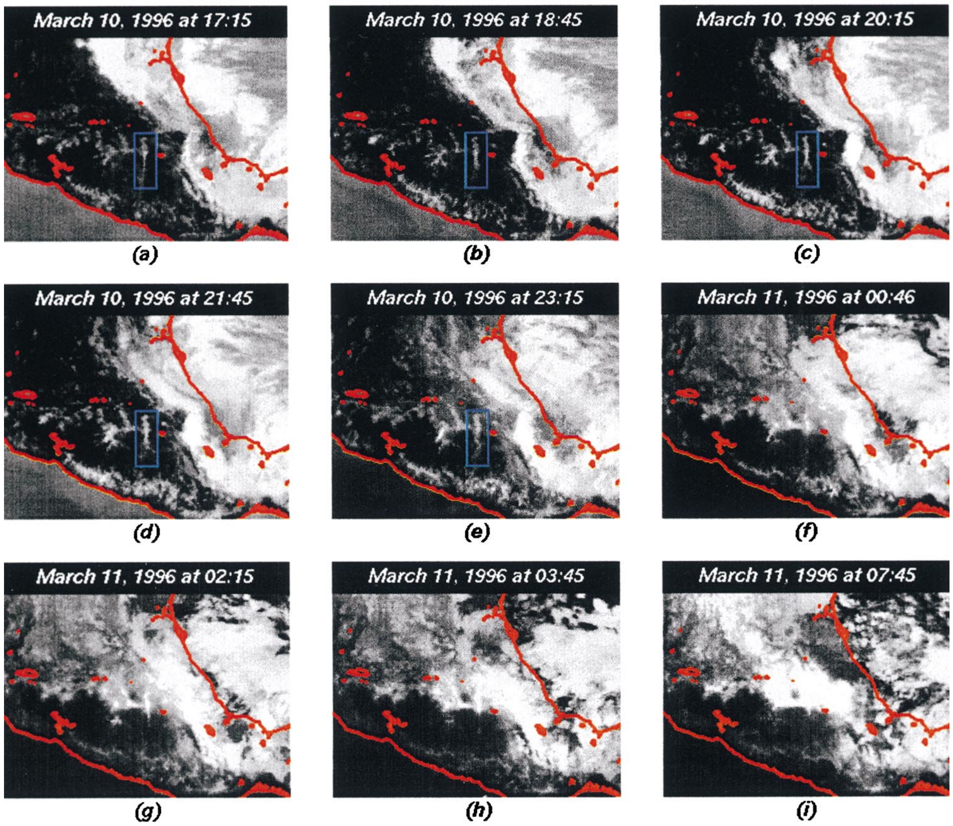

Volcanic Ash Detected by the T_4 – T_5 Subtraction Algorithm (e.g., Schneider and Rose, (1995))

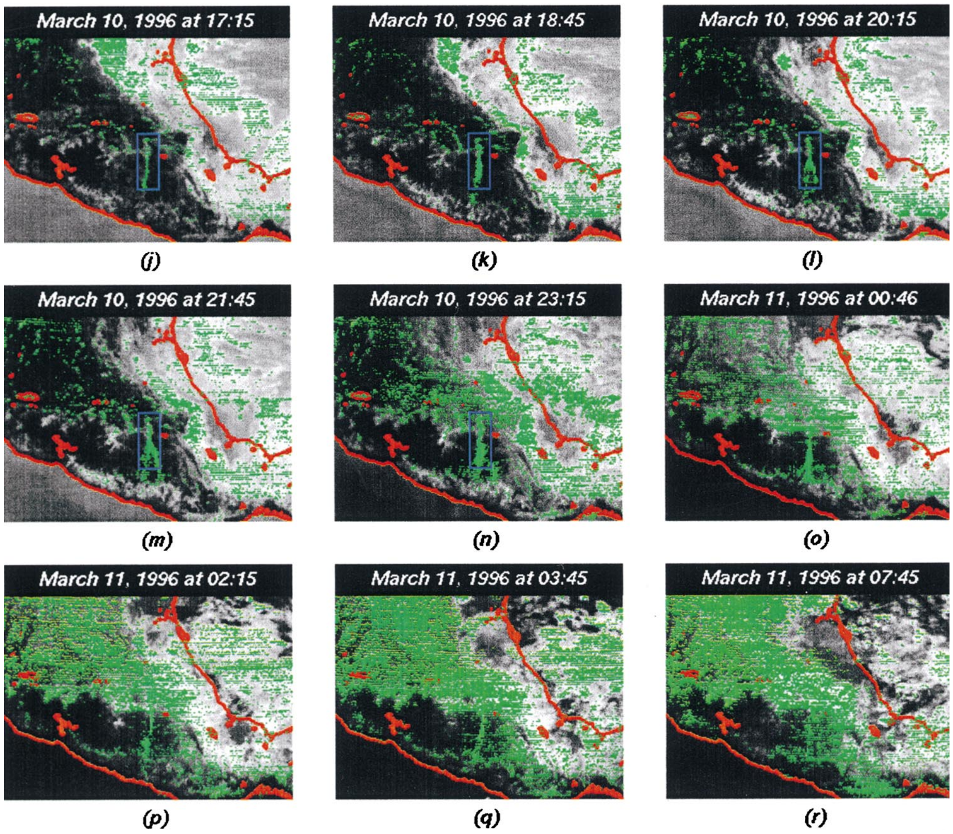

Figure 11. Panels a–i illustrate a time series of nine GOES-8 T_4 images for the Popocatepetl, Mexico eruption. Coastlines are orange. The blue boxes in panels a–e bracket the volcanic plume. Green overlays show location of pixels assigned to the volcanic ash cloud class by the $T_4 - T_5$ algorithm in panels j–r. Gross false classification of meteorological cloud as volcanic ash cloud occurs for this sequence of images.

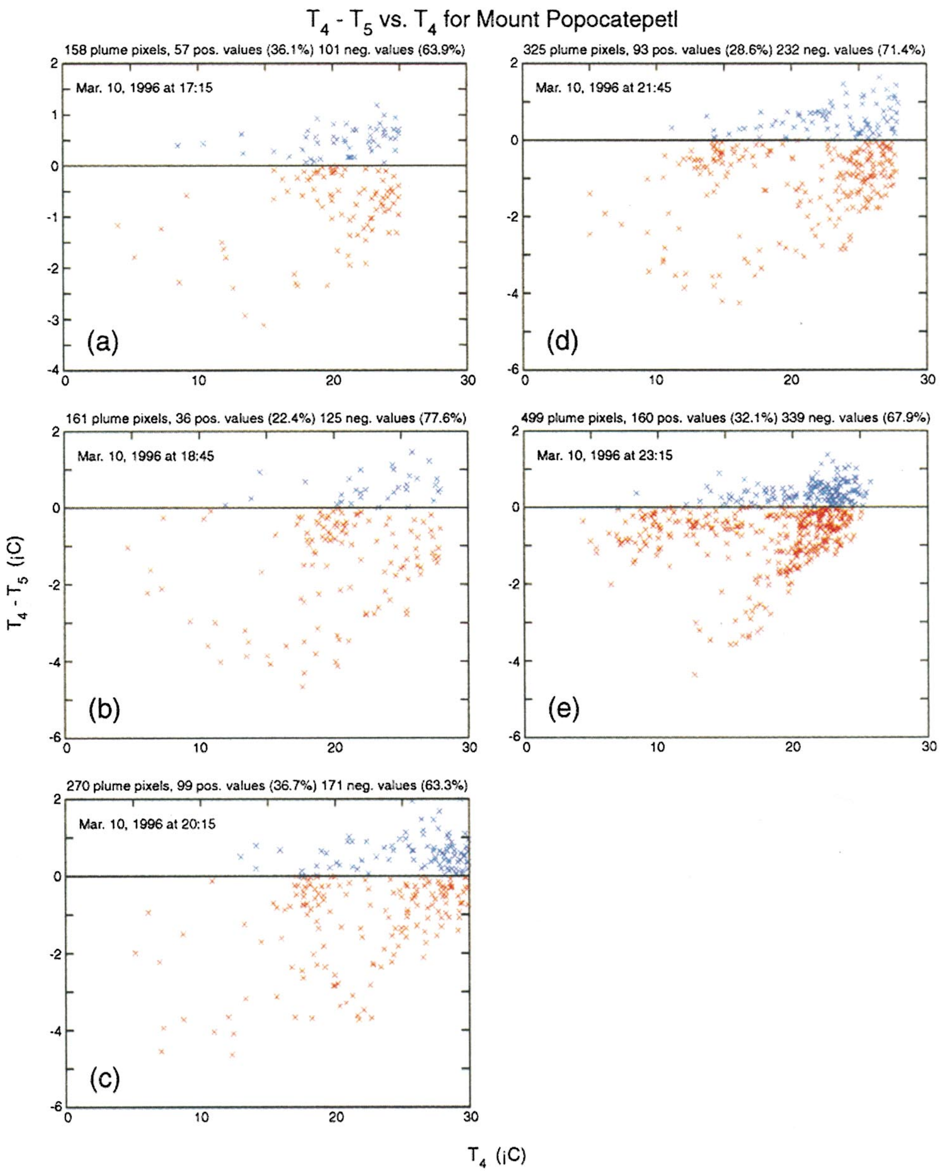

Figure 12. Analogous to Figure 4, except there is a direct correspondence between panels a–e and j–n in Figure 11, and those herein.

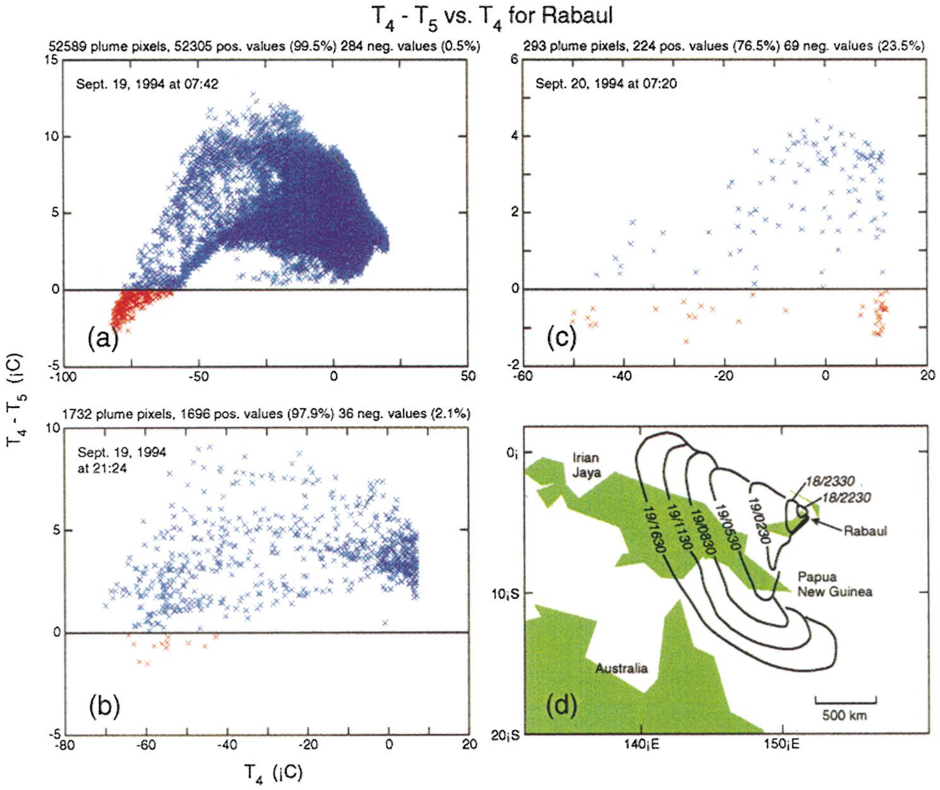

Figure 13. Panels a–c show plots of T_4-T_5 versus T_4 for pixels in the volcanic plume of the Rabaul eruption. Blue X's correspond to classification of volcanic ash pixels as meteorological clouds. Panel d shows the extent of the volcanic ash cloud as a function of data/time curves based on an independent analysis of the Smithsonian Institution's Global Volcanism Program. Clearly, the T_4-T_5 volcanic ash detection procedure failed catastrophically for this eruption.

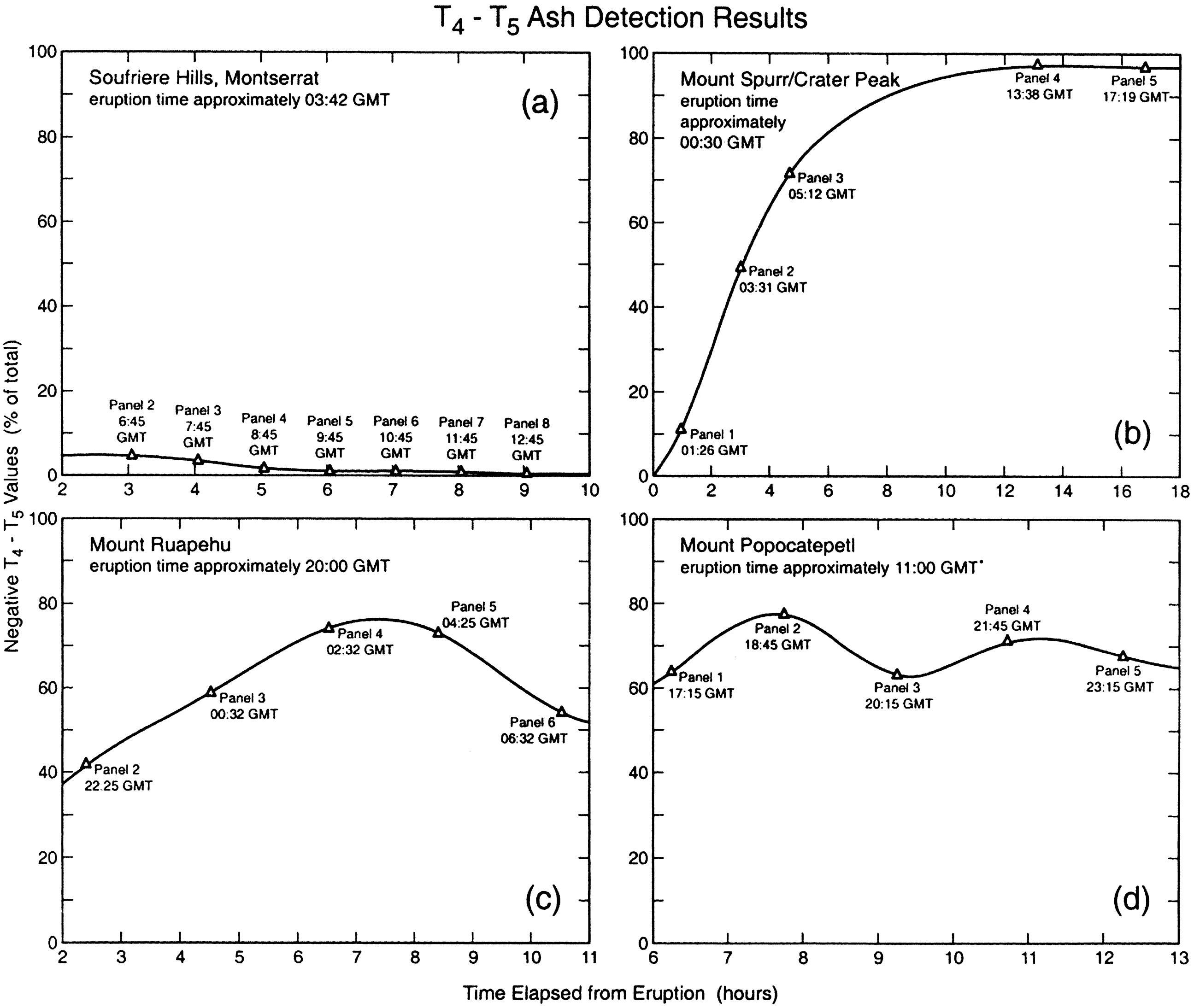

Figure 14. Plot of percent negative T_4-T_5 pixels in the volcanic ash plume (hence correctly classified as volcanic ash plume) as a function of time since eruption. 100% negative T_4-T_5 means correct classification of all pixels within the volcanic ash plume. Panel a corresponds to the Montserrat eruption. The best result achieved only had a 4.5% correct classification accuracy. Nine hours after the eruption the classification accuracy was only 0.4%. Panel b is analogous to panel a except for the Mount Spurr/Crater Peak eruption. High accuracy of plume detection only is achieved many hours after the event. c) and d) are for the Mount Ruapehu and Popocatepetl eruptions, respectively. The oscillatory behavior in the classification skill is partly due to intermittency in eruptive activity within the time horizon of a given event.

in the scene and often misclassifies meteorological clouds as volcanic ash. The presence of water vapor in the erupting column (e.g., moist tropical atmospheric conditions; phreatic eruption processes that are essentially steam driven; phreatomagmatic eruptions that involve interaction between external water and the magma) produces conditions which compromise the T_4-T_5 test. This can result in catastrophic failures of the T_4-T_5 algorithm (e.g., Fig. 14a), result in a long elapsed time between the actual explosive event and the time that a reliable volcanic ash plume signature is discernable in the satellite data (Figure 14b), and/or produce oscillatory performance in the T_4-T_5 algorithm's classification skill (Figs. 14c and 14d). Multiple eruption pulses within a given cycle often can explain the oscillatory behavior in classification skill as each pulse can release more surface and/or ground water and juvenile water into the eruptive column and/or entrain more ambient atmospheric water vapor. These results demonstrate that the T_4-T_5 test for volcanic ash detection, especially during the early stages of an eruption, is not an ideal tool.

Radiative Transfer Calculations

The effects of aerosol contamination on the transmittance of radiation observed by a satellite were investigated using aerosol models taken from MODTRAN (Berk and Bernstein, 1989) and a radiative transfer model developed by Stamnes et al. (1988). In MODTRAN, the volcanic aerosol is classified as stratospheric aerosol (for heights between 10 km and 30 km). There are four different vertical profiles of extinction coefficients for background, moderate, high, and extreme volcanic aerosol loading situations, which represent various stages in the evolution of the stratospheric aerosol layer after a volcanic eruption. The optical properties for the volcanic aerosols are given at only 47 individual wavelengths from UV to microwave (.2000, .3000, .3371, .5500, .6943, 1.0600, 1.5360, 2.000, 2.2500, 2.5000, 2.7000, 3.0000, 3.3923, 3.7500, 4.5000, 5.0000, 5.5000, 6.0000, 6.2000, 6.5000, 7.2000, 7.9000, 8.2000, 8.7000, 9.0000, 9.2000, 10.0000, 10.5910, 11.0000, 11.5000, 12.5000, 14.8000, 15.0000, 16.4000, 17.2000, 18.5000, 21.3000, 25.0000, 30.0000, 40.0000, 50.0000, 60.0000, 80.0000, 100.000, 150.000, 200.000, 300.000 μm). The size distributions are represented by a modified gamma distribution. These data can be used to calculate the optical properties of a specified aerosol type in each atmospheric layer and in each spectral band for the radiative transfer computations by interpolation.

In the computation of transmittance of volcanic aerosols, the coefficients of spectral extinction and absorption and the vertical distribution profiles for volcanic aerosols in the atmosphere were taken from the MODTRAN database. From these data, the optical depth of the volcanic aerosol in each layer can be calculated, and therefore the total optical depth, τ, can be obtained. Then, the transmittance T is simply calculated by Eq. (2):

$$T = \exp(-\tau). \tag{2}$$

Therefore, this is basically the beam transmittance through one vertical atmospheric path, which might be different from some other definitions.

Figure 15 shows modeled transmittance as a function of wavelength for moderate, high, and extreme volcanic aerosol concentrations based on the available MODTRAN data. The vertical bars in this figure show the location of the central wavelength of the five bands on the AVHRR instrument (marked $A_1, \ldots, A_5$, respectively) and the corresponding wavelengths for GOES-8 (marked $G_1, \ldots, G_5$, respectively). For the AVHRR case, the moderate and high volcanic aerosol loadings have negligible effect on the transmittance in the thermal infrared bands centered at 10.8 μm and 12.0 μm and the mid-infrared band centered at 3.75 μm. In fact, for these aerosol loadings, even the 0.63 μm and 0.92 μm bands show only limited effects on their respective transmittance. For extreme volcanic loading, maximum effect in transmittance in the thermal infrared occurs near 8.9 μm, however, the visible, near- and shortwave-infrared bands show greater sensitivity. These radiative transfer calculations are consistent with the observational results (Figs. 4, 6, 8, 10, 12, and 13) and further demonstrate that neither the 11 μm nor 12 μm channels on currently flying operational satellites are ideally suited for volcanic ash detection. Given the inherent lack of sensitivity of these channels to volcanic ash aerosols and the highly variable water vapor effects documented herein, it can be concluded that, in general, a T_4-T_5 difference will not be an optimum detector of the volcanic ash associated with an arbitrary eruption. Similar conclusions can be drawn about the GOES-8 channels.

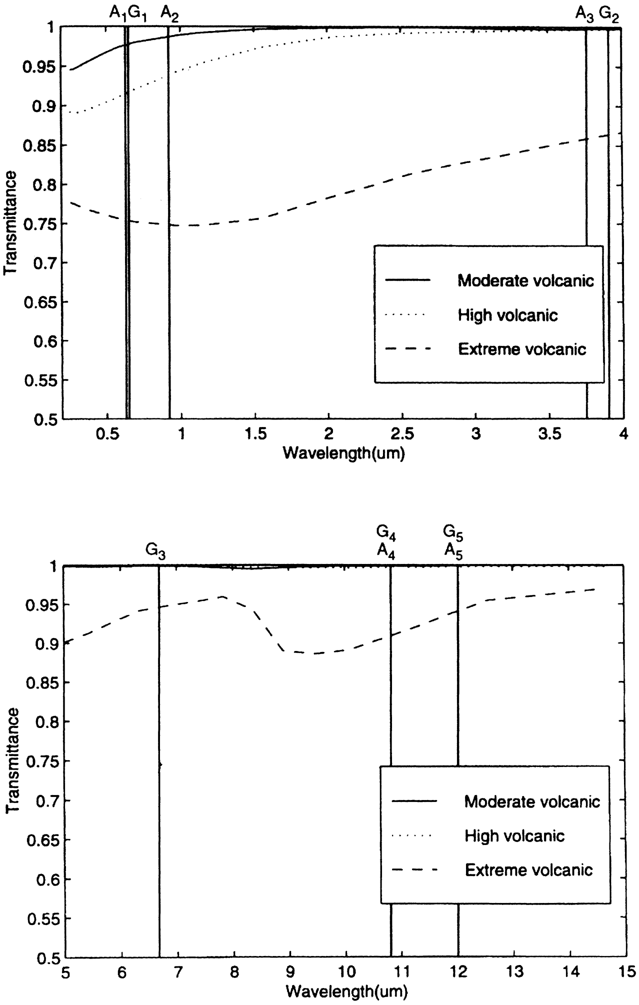

Figure 15. Transmittance as a function of wavelength computed for three different aerosol concentrations using the volcanic aerosol models of MODTRAM. Central wavelengths of AVHRR (A_i) and GOES (G_i) Channels $i=1$–5 are also indicated by vertical lines.

Failure Modes of Detection

Volcanic Ash Clouds as Meteorological Cloud

Limitations of the T_4-T_5 algorithm in discriminating volcanic and meteorological cloud have been recognized by others. Prata (1989a,b) found that, for ice-free ash clouds with particles of mean radii less than 3 μm, T_4-T_5 differ-

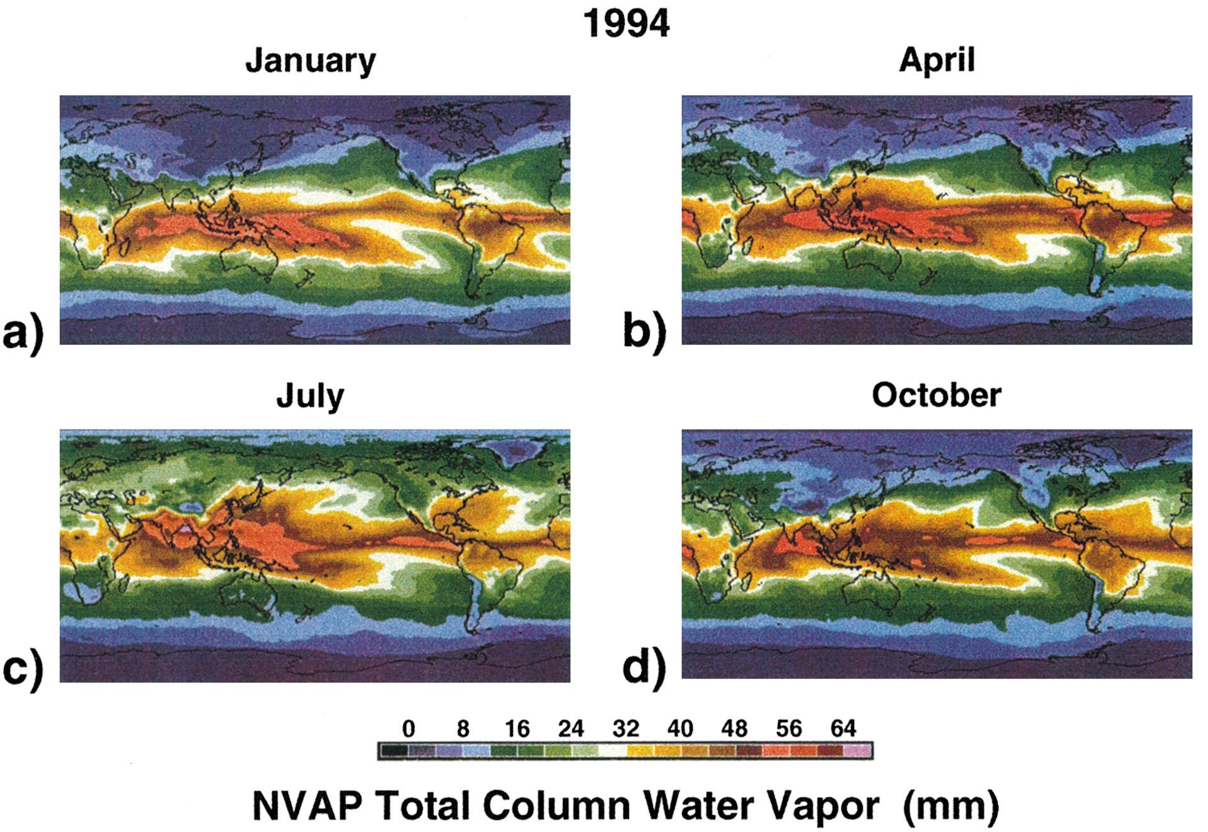

Figure 16. Typical (1994) global distributions of mean monthly atmospheric water vapor for a) January, b) April, c) July, and d) October. Source of data is NASA's Water Vapor Project.

Figure 17. Global distributions (mercator projection) of active volcanoes around the world which potentially pose a threat to modern aviation. Data source is the Smithsonian Institution's Global Volcanism Program (http://www.volcano.si.edu/gvp).

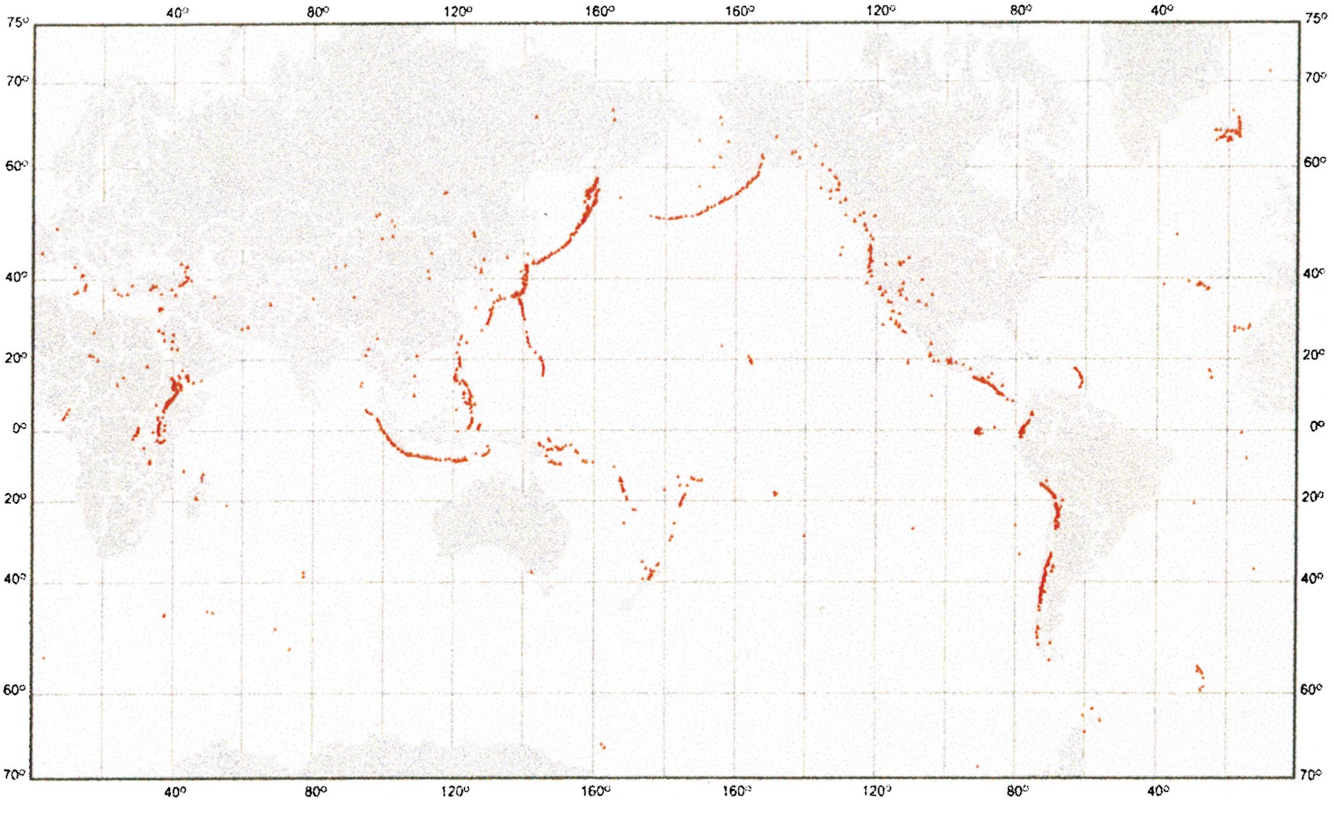

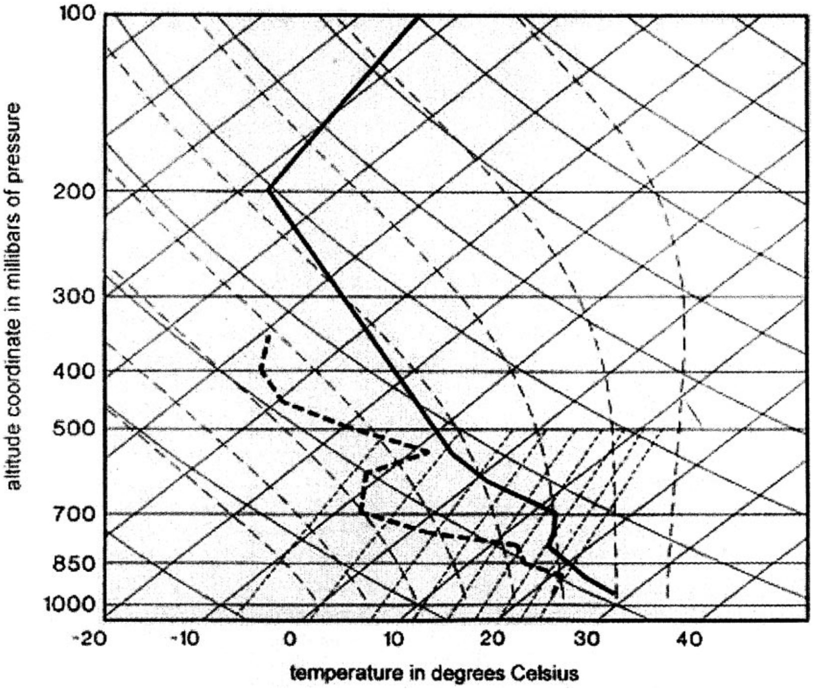

Figure 18. Simplified Skew-T plot. A complete description of the Skew-T plot and its interpretation is given in the Appendix.

ence will be negative. However, when the mean radii was equal to or greater than 3 μm, the ΔT may be positive. In addition, as the fraction of ice increases in the ash cloud, then ΔT becomes even more positive; consistent with the spectral characteristics of ice (Volz, 1972; Irvine and Pollack, 1968; Prata, 1989b). In examining AVHRR imagery of the Mt. Pinatubo ash clouds, Potts (1993) found positive T_4-T_5 differences where the ash cloud was coldest and thickest.

Volcanic ash clouds associated with a large moisture source often result in positive T_4-T_5 differences. The Montserrat event is a dramatic case, demonstrating the inability to detect an ash cloud associated with high quantities of water vapor (Fig. 14a). Seasonal global total column water vapor (Fig. 16) shows that there are many regions, especially the tropical and subtropical areas, where atmospheric water vapor concentrations are high enough that when entrained into the eruptive column, the moisture will "mask" the presence of volcanic ash.

The Ruapehu eruption is an excellent example where the volcanic ash cloud contained large quantities of surface and ground water (Christenson et al., 1992); about an order of magnitude greater in this eruption than in the other five cases. Rose et al. (1995) found that in a cloud composed of a mixture of ash and water/ice particles, or when an ice cloud overlies an ash cloud, negative differences may not be observed, and the positive values were misinterpreted as meteorological clouds free of ash.

The presence of copious amounts of water, water/ice, and ice in a mixture of ash can often result in positive T_4-T_5 differences. This would result in the cloud being interpreted as a meteorological cloud.

Meteorological Clouds as Volcanic Ash Clouds

In the tropical Indonesian region, T_4-T_5 negative differences can occur at very cold convective cloud top temperature when no volcanic ash is present (Potts and Ebert, 1996). They attribute the "false alarm" to overshooting tops of convective clouds which penetrate the tropical tropopause and are capped by a strong temperature inversion at the top of the cloud layer. Temperatures as cold as 173 K have been observed (Ebert and Holland, 1992). In such a case, a T_4-T_5 signature would be negative if the majority of radiation at Channel 5 (11.9 μm) emanates from a higher level, at a warmer temperature, due to a differential absorption. This would lead one to suggest the presence of volcanic ash in the cloud when there is none.

Misclassifications of meteorological cloud as volcanic ash cloud, however, are not simply confined to the tropics. The March 1986 Mt. Augustine eruption in Alaska, for example, provides additional evidence of this mode of misclassification (Fig. 7, panels e–h). Radiosonde data (analyzed but not shown) indicate that the atmospheric temperature generally was colder than −50°C at heights greater than 12 km. The height of the volcanic ash plume varied between 11.6 km and 14.3 km during the eruption. Thus, much of the false detection (Fig. 7, panels e–h) is probably associated with very cold brightness temperatures observed by the satellite, consistent with the hypothesis of Potts and Ebert (1996). Moreover, the presence of snow colder than −40°C on cloud-free land, probably enhanced the false detection rate of the T_4-T_5 algorithm in this case in a fashion analogous to that described by Potts and Ebert (1996).

Global Atmospheric Water Vapor Distribution

NASA's Water Vapor Project (NVAP) assembled the best available observations of global atmospheric water vapor [e.g., data from the global radiosonde network, satellite retrievals from the Special Sensor Microwave/Imager (SSM/I) and from the TIROS Operational Vertical Sounder (TOVS)] and blended these data into a global water vapor product (Randel et al., 1996). Mean total column water vapor for the months of January, April, July, and October 1994 are shown in Figure 16, panels a–d, respectively. These data were chosen as representative of a typical year (neither a strong ENSO nor La Niña period). The months were selected to illustrate important seasonal differences in the water vapor distributions. All data share a common scale (0–68 mm) for easier interpretation of seasonal and/or geographical differences in the global distributions.

In January (Fig. 16a), the polar atmosphere is very dry. Typical values of total column water vapor for Alaska and Kamchatka are between 0 mm and 8 mm. The tropical Caribbean and Mexico have their lowest values for the annual cycle (9–34 mm, depending on the specific location). In the Indonesian region, total column water vapor is high compared to most other areas on earth. Values range from 48 mm to 56 mm and again are location sensitive. In April (Fig. 16b), the polar atmosphere is still quite dry. The Caribbean and Mexico regions, however, have a relatively moist atmosphere compared to that in January, and the Indonesian region shows the development of a major core area with very high total column water vapor.

By July (Fig. 16c), the polar atmosphere is considerably moister than in January. Total column water vapor for Alaska and Kamchatka now varies between 16 mm and 28 mm. The coastal regions of Japan, Korea, and China are much moister in summer than in winter (Fig. 16a). The high moisture area over Indonesia in January through April now has moved northwest towards southeast Asia and India. Nonetheless, the Indonesian region still has a moist atmosphere with total column water vapor ranging from about 32 mm to 52 mm, depending on the location.

In October (Fig. 16d), the total column water vapor patterns are beginning to revert to their wintertime distributions. Once again, the polar regions are relatively dry. India and Southeast Asia also have drier atmospheres compared to July. The Caribbean and parts of Mexico still have relatively moist atmospheres, and the very high zone of total column water vapor over Indonesia and the western tropical Pacific is beginning to reestablish itself.

The regional and seasonal variation in total column water vapor (Fig. 16), coupled with the failure modes of the T_4-T_5 volcanic ash detection procedure discussed above, indicate that space/time variation in atmospheric water vapor may partially explain why the T_4-T_5 detection procedure may work to some degree for a given eruption and then fail for a different eruption of the same volcano during a wetter season.

CONCLUSIONS

Global Implications

Subaerial volcanic eruptions can happen anytime, in just about any region of the globe, as there are currently active volcanoes on every continent, except Australia, and across the world's ocean basins (Fig. 17). These volcanoes pose a threat to aviation. Thus, explosive volcanic eruptions typically will inject volcanic aerosols into a variety of atmospheric conditions that reflect geographic and temporal variabilities with respect to the global distribution of water vapor (Fig. 16). Because the radiometric remotely-sensed detection of volcanic plumes can be profoundly modified by ambient atmospheric conditions (Figs. 3–14), it becomes crucial, from an operational standpoint, to understand how these globally variable water vapor regimes affect plume detection thresholds.

Given that most of the world's volcanoes have been generated by the dissipation of thermal energy associated with the subduction of the oceanic plates over geologic timescales, most of the world's active volcanoes are in close proximity to marine environments, if not islands themselves (Fig. 17). Thus, whenever explosive eruptions inject volcanic products through or into maritime weather systems, the difficulty of differentiating these plumes from meteorological clouds is increased markedly.

The maritime condition, though significant at all latitudes, becomes particularly troublesome in the tropics. Vertical atmospheric water vapor fluxes over sea and land are greatly increased in tropical zones, as higher temperatures cause higher evaporation rates and increased tropospheric convective activity (e.g., thunderstorms). Also, the vertical extent of convective activity is much greater in tropical zones because the tropopause is a factor of 2 (or possibly 3) higher there than in arctic and subarctic regions. Thus, the T_4-T_5 detection of evolved tropospheric and stratospheric volcanic ash plumes in the tropics (e.g., the current Montserrat eruption series) is fundamentally compromised because of the typical presence of so much water vapor under a very high tropopause.

In addition, seasonal variability can compound the detection problem. For instance, in the case of Volcano Popocatepetl near Mexico City, for midsummer eruptions, typical weather patterns will generally transport ash to the west and southwest, under conditions that will be generally cloud-free and dry. Midwinter eruptions, however, most often will result in ash transport toward the east and northeast over the Caribbean region into the mid-Atlantic toward Bermuda, through typically very humid and cloudy conditions (Fig. 16; Stunder, 1999; Pieri, 1998). World-wide, such seasonal variability is endemic. For instance, monsoon versus dry season water vapor variability will significantly degrade the detectability of volcanic plumes during wet times of the year (Fig. 16). Seasonal variation in atmospheric water vapor over Alaska also may have contributed to differences in the success of T_4-T_5 volcanic ash detection for the Mt. Augustine (March 1986) and the Mt. Spurr/Crater Peak (August 1992) eruptions. Some of the false detection in the later stages of the Mt. Spurr/Crater Peak eruption (Fig. 5, panels i and j), for example, may be associated with the higher water vapor content in the summer atmosphere over Alaska.

To be effective, the T_4-T_5 technique demands that the eruption plume be translucent to upwelling thermal IR radiation from the earth. Otherwise, volcanic clouds (i.e., water vapor+ash+volcanic gases) are just as opaque at thermal wavelengths as are pure water vapor clouds. Thus, particularly under very humid conditions, there is a latency period before the volcanic plume can be detected, which is the time it takes for the thermal IR optical depth of the volcanogenic cloud to drop below unity. Thus, confident detection of a volcanogenic cloud that has begun to "clear" may take up to several hours. This is a crucial and unacceptable delay from the standpoint of airline operations, and can contribute to significant uncertainties in ash trajectory forecasts (e.g., VAFTAD, CANERM). Thus, plume detection schemes such as the T_4-T_5 "split window" technique are fundamentally incapable of providing prompt detection of the explosive eruption event itself, except in the most ideal dry and clear conditions.

Clearly, the most pressing need for prompt eruption and plume detection are in areas where heavy commercial air traffic is juxtaposed with high active volcanic areas. Two such areas are the North Pacific Rim (i.e., Cook Inlet Volcanoes of Alaska, Aleutian Islands, Kamchatka Peninsula, Kurile Islands, and Japan) and the South Pacific Rim (i.e., Philippines, Papua New Guinea, Borneo, Indonesia, and New Zealand). Unfortunately, these areas have strong maritime climates, with typically very cloudy conditions and high relative humidity, at least during some seasons (Fig. 16). Thus, it will take a combination of strong future *in situ* volcano monitoring programs, combined with improved and optimized remote sensing instrumentation and algorithms, to provide the margins of safety that airline passengers deserve.

Operational Implications

Present global air routes put commercial jet aircraft into direct proximity of many volcanoes capable of injecting volcanic ash into the atmosphere. Moreover, many of these volcanoes are located in remote locations and are not instrumented. The ash hazard is most acute when airborne ash concentration is highest, during the initial eruption. Jet aircraft today move at approximately 12.8 km/min. Immediate warning notification is imperative to those aircraft moving toward the ash plume if they are to avoid severe risk to passengers and equipment.

To provide a timely and accurate warning and/or advisory, the operational forecaster needs the following information: 1) time and location of the eruption; 2) vertical and horizontal extent of the eruptive column; 3) rapid and accurate detection of the airborne ash; and 4) winds at the ash injection altitude. Results presented herein show that accurate and early detection of airborne volcanic ash by satellite remote sensing may not occur using present techniques. If the T_4-T_5 technique is fortunate to detect some airborne ash, the forecaster must subjectively "draw a large box" around the area where ash is suspected for safety reasons. This puts a large burden on the aircraft crew to fly many miles around the estimated hazard area, increasing flight time and length of flight, and directly affecting fuel consumption. The majority of commercial jet aircraft transiting the North Pacific air routes are carrying cargo. To maximize profits, fuel may be reduced so that they can carry more cargo. These aircraft can become severely handicapped by unanticipated extended flight. The forecaster may have to wait a number of hours before they can obtain sufficient accurate information to reduce the area of the hazard.

Towards Better Detection

The detection and discrimination of volcanic plumes using multispectral remote sensing is a complex problem involving the radiometry of a multicomponent, multiphase aerosol. Given that the current fleet of available operational remote sensing instruments from the United States and abroad (e.g., AVHRR, GOES, GMS, METEOSAT, etc.) are designed for the detection and mapping of meteorological clouds, it should not be surprising that the volcanic ash plume detection problem strains the effectiveness of current systems.

Nevertheless, using meteorological satellites, much has been learned over the last 20 years about the spectral character of volcanic eruption plumes, and the T_4-T_5 "split window" technique. Despite shortcomings documented here, it remains the most useful, currently available tool for operational tracking of volcanic plumes during the night and for mid and high level events. For evolved translucent plumes in the stratosphere that are more than a day old, this technique may work some of the time. But for the time period right after the eruption event through the first several hours, and ranging up through the first day, this simple technique is not universally effective over the wide range of atmospheric and volcanologic conditions that pertain. In addition, this technique is strongly dependent on aerosol particle size-frequency distribution, as the scattering by large aerosol particles (>3 μm) is likely to produce a positive T_4-T_5 signature.

The key to better volcanic ash detection lies in designing better future instruments which optimizes volcanic ash detection. Such a program should combine the following four elements: a) laboratory spectrophotometric observations under controlled conditions of simulated volcanic plumes, in order to explore more fully their parameter space; b) *in situ* measurements of water vapor and ash particulate concentrations and distributions of volcanic plumes, combined with simultaneous aircraft and/or satellite-borne spectrophotometry; c) effectively using new research-grade satellite remote sensing instruments that will be available (e.g., MODIS, ASTER, ENVISAT) for the provision of multispectral observations of volcanic plumes in the thermal IR wavelength band to better characterize eruptive events (this new information can be used to design improved volcanic ash cloud detection sensors); and d) using sound radiative transfer models, in conjunction with the aerosol information obtained from components a, b, and c, to better model instrument response and help determine the best retrieval methods for improved volcanic ash identifications. The goal of these observations and models should be to better refine and elaborate our still somewhat limited knowledge of the spectral characteristics of volcanic ash plumes over a wide variety of environmental conditions. Only then can we implement an optimal design strategy for the next generation of instruments which should have the capability to effectively observe volcanic phenomena.

APPENDIX: RADIOSONDE DATA AND THE SKEW-T DIAGRAM

Upper air soundings are obtained using a radiosonde instrument carried aloft by balloons to measure pressure, temperature, and humidity and simultaneously transmit the recorded data (Lally, 1985). Winds are determined by an instrument located on the ground that tracks the radio signal transmitted by the radiosonde. The World Meteorological Organization sets accuracy requirements and performance limits for the radiosonde instruments. Pressure must be measured to an accuracy of ±1 mb (1 mb=1 hPa), temperature to an accuracy of ±0.5°C, and relative humidity to an accuracy of ±5%.

A Skew-T, Log *P* thermodynamic diagram, commonly called the Skew-T plot, is the most common plot used by the operational meteorological forecaster to display and analyze data from the balloon radiosonde sounding. Figure 18 shows a simplified version of the Skew-T with plotted data for demonstration purposes. The horizontal axis of the plot is the temperature (°C), and the vertical axis is a scale of inverse logarithmic atmospheric pressure in millibars (mb). The sounding temperatures are plotted on a backdrop grid that slants to the right with height relative to the horizontal and vertical axis. This is done so that the measured temperature, as it decreases with altitude under normal cooling rates, will show up as nearly a vertical line. The measured air temperature is always plotted to the right on the graph as a heavy solid line, while the dew-point temperature, a measure of humidity, is plotted to the left as a heavy dashed line. The grid consists of curving solid lines that represent dry adiabatic lapse rate (10°C/km), long dashed curved lines representing the moist adiabatic lapse rate (4–9°C/km), and short, dashed straight lines that represent lines of constant mixing ratio (g water vapor/kg dry air).

Often winds are plotted as wind barbs with height on the right edge of the Skew-T diagram (not shown). In addition specific sounding-related parameters are plotted in an upper left-hand corner (not shown). Some of these parameters include height of the tropopause level (mb), precipitable water (in.), lifting condensation level (LCL) in mb, lowest freezing level (mb), and a number of indices for potential lift of a parcel. See Lally (1985) for a complete list and description of the sounding parameters.

The Skew-T diagram provides an important means for determining the stability of the atmosphere above a specific location for both unsaturated and saturated air (Doswell et al., 1991) The theoretical movement of air on a Skew-T diagram uses the concept of a parcel. If a parcel of air at any height along the measured sounding is forced upward, it will expand and cool at a rate prescribed by the dry adiabatic lapse rate. The projected temperature of the parcel off the sounding is traced along or parallel to a dry adiabat. If the resultant parcel temperature is colder than the surrounding environment, its density will be greater, and the parcel will resist further upward movement and tend to sink to a lower level, where its temperature (and density) is the same as the surroundings. This produces a stable condition in the atmosphere because the parcel resists change. If the resultant parcel temperature is warmer than its surroundings, the less dense parcel will be buoyant and will continue to accelerate upward. This condition is considered unstable because the parcel is prone to move upward. If a parcel moves up or down in a fashion equivalent to the environmental sounding temperature profile at the dry adiabatic lapse rate, then it will tend to stay at the level to which it is moved, producing a neutral stability.

When a parcel of saturated air is lifted, condensation takes place and releases latent heat. Now instead of cooling at a dry adiabatic lapse rate, the addition of latent heat offsets the cooling. The new rate of cooling of the parcel, the moist adiabatic lapse rate represented on the Skew-T as the long dashed curved lines, will be slower as long as the parcel remains saturated.

This work was sponsored by the Marine Life Research Group of the Scripps Institution of Oceanography and a NOAA grant from the U.S. National Weather Service. G. Hufford was supported by NOAA/NWS directly. D. Pieri was supported by the

Jet Propulsion Laboratory under contract to the NASA Solid Earth and Natural Hazards Program, the NASA EOS Project (ASTER and Volcanology-IDS Teams), and by the NASA Earth Science Technology Office. Z. Jin performed the MODTRAN/radiative transfer calculation. J. Ashton and M. Azgour assisted with manuscript preparation. G. Tapper assisted with final figure preparation. P. Borey proofread the manuscript.

REFERENCES

Berk, A., and Bernstein, L. S. (1989), MODTRAN: A Moderate Resolution Model for LOWTRAN7, Report AFGL-TR-89-0122, Air Force Geophysical Laboratory, Hanscom Air Force Base, MA.

Bluth, G., Scott, C. J., Sprod, I. E., Schnetzler, C. C., Kureger, A. J., and Walter, L. S. (1995), Explosive emissions of sulfur dioxide from the 1992 crater peak eruptions Mount Spurr Volcano, Alaska. In *The 1992 Eruptions of Crater Peak Vent*, Mount Spurr Volcano, Alaska (T. Keith, Ed.), USGS Bull. 2139, U.S. Geological Survey, Washington, DC, pp. 37–46.

Campbell, E. E. (1994), Recommended flight-crew procedures if volcanic ash is encountered. *U.S. Geol. Surv. Bull.* 2047:151–157.

Cas, R. A. F., and Wright, J. W. (1987), *Volcanic Successions, Modern and Ancient*, Allen and Unwin, London, 487 pp.

Casedevall, T. (1994), Perspectives on the hazards of volcanic ash. In *First International Symposium on Volcanic Ash and Aviation Safety*, USGS Bull. 2047, U.S. Geological Survey, Washington, DC, pp. 1–6.

Christenson, B. W., Crump, M. E., and Glover, R. B. (1992), Ruapehu Crater Lake bathymetry, temperature profile and water column chemistry: February 1991. In *Proc. Int. Symp. on Hazardous Crater Lakes*, Misasa and Tateyama, Japan, pp. 25–29.

Davies, M. A., and Rose, W. I. (1998), GOES imagery fills gaps in Montserrat volcanic cloud observations. *E.O.S.* 79: 505–507.

Doswell, C. A., Anderson, L. C., and Imy, D. A. (1991), *Basic Convection I: A Review of Atmospheric Thermodynamics*, NOAA-NWS Report, National Weather Service Office, Norman, OK.

Doukas, M., and Gerlach, T. (1995), Sulfur dioxide scrubbing during the 1992 eruptions of Crater Peak, Mount Spurr Volcano, Alaska. In *The 1992 Eruptions of Crater Peak Vent, Mount Spurr Volcano, Alaska* (T. Keith, Ed.), USGS Bull. 2139, 220, U.S. Geological Survey, Washington, DC, pp. 47–58.

Ebert, E. E., and Holland, G. (1992), Observations of record cold cloud-top temperatures in Tropical Cyclone Hilda (1990). *Mon. Weath. Rev.* 120:2240–2251.

Fisher, R. V., and Schmincke, H. U. (1984), *Pyroclastic Rocks*, Springer-Verlag, Berlin, 472 pp.

Fox, T. (1988), Global airways volcano watch is steadily expanding. *ICAO Bull.* April:21–23.

Glaze, L. S., Baloga, S. M., and Wilson, L. (1997), Transport of atmospheric water vapor by volcanic eruption columns. *J. Geophys. Res.* 102(D5):6099–6109.

Haltner, G. J., and Martin, F. L. (1957), *Dynamical and Physical Meteorology*, McGraw-Hill, New York, 470 pp.

Hamilton, D. L., Burnham, C. W., and Osborn, E. F. (1964), The solubility of water and effects of oxygen, fugacity and water content on crystallization in mafic magmas. *J. Petrol.* 5:21–39.

Heiken, G. (1994), Volcanic ash: what it is and how it forms. *U.S. Geol. Surv. Bull.* 2047:39–45.

Holasek, R. E., and Rose, W. I. (1991), Anatomy of 1986 Augustine volcano eruptions as recorded by multispectral image processing of digital AVHRR weather satellite data. *Bull. Volcanol.* 53:420–35.

Houghton, D. D. (1985), *Handbook of Applied Meteorology*, Wiley-Interscience, New York, 1461 pp.

Irvine, W. M., and Pollack, J. B. (1968), Infrared optical properties of water and ice. *Icarus* 8:324–360.

Krueger, A. J., Walter, L. S., Bhartia, P. K., et al. (1995), Volcanic sulfur dioxide measurements from the total ozone mapping spectrometer instruments. *J. Geophys. Res.* 100:14, 057–14,076.

Lally, V. E. (1985), Upper air *in situ* observing systems. In *Handbook of Applied Meteorology* (D. D. Houghton, Ed.), Wiley, New York, pp. 352–360.

Moran, J. M., and Morgan, M. D. (1997), *Meteorology: The Atmosphere and the Science of Weather*, Prentice-Hall, Englewood Cliffs, NJ, 530 pp.

NOAA (1979), Data Extraction and Calibration on Tiros-N/NOAA Radiometers. NOAA Technical Memorandum NESS/107, Washington, DC, pp. 58 and Appendices.

NOAA (1981), *Radiosonde Observations*, Federal Meteorological Handbook No. 3, U.S. Department of Commerce, Washington, DC.

Pieri, D. C. (1999), Precursor monitoring, eruption detection, and aerosol tracking: integrating in-situ and remote sensing techniques. In *Proceedings of the JUST Workshop on the Utilization of Remote Sensing Technology for Natural Disaster Reduction*, 26–28 October 1998, Tsukuba, Japan.

Potts, R. J. (1993), Satellite observations of Mt. Pinatubo ash clouds. *Aust. Meteorol. Mag.* 42:59–68.

Potts, R. J., and Ebert, E. E. (1996), On the detection of volcanic ash in NOAA AVHRR infrared satellite imagery. In *8th Australasian Remote Sensing Conference*, Canberra, Remote Sensing and Photogrammetry Association Australia, Ltd., Floreat, Western Australia, March, pp. 25–29.

Prata, A. J. (1989a), Observations of volcanic ash clouds using AVHRR-2 radiances. *Int. J. Remote Sens.* 4:751–761.

Prata, A. J. (1989b), Infrared radiative transfer calculations for volcanic ash clouds. *Geophy. Res. Lett.* 16:1293–1296.

Randel, D. L., Vonder Haar, T. H., Ringerud, M. A., Stephens, G. L., Greenwald, T. J., and Comb, C. L. (1996), A new global water vapor data set. *Bull. Am. Meteorol. Soc.* 77: 1233–1246.

Robertson, R., Cole, P., Sparks, R. S. J., et al. (1998), The explosive eruption of Soufriere Hills Volcano, Montserrat, 17 September 1996. *Geophys. Res. Lett.* 25:3429–3432.

Rose, W. I., Lostinski, A. B., and Kelley, L. (1995), Real-time C-band radar observations of 1992 eruption clouds from Crater Peak, Mount Spurr Volcano, Alaska. In *The 1992 Eruptions of Crater Peak Vent, Mount Spurr Volcano, Alaska* (T. Keith, Ed.), USGS Bull. 2139, 220, U.S. Geological Survey, Washington, DC, pp. 19–27.

Schartz, B. E., and Govett, M. (1992), A hydrostatically consistent North American radiosonde database at the Forecast

Systems Laboratory, 1946–present, NOAA Technical Memo. ERL FSL-4, NOAA/ERL/FSL, Boulder, CO.

Schneider, D. J., and Rose, W. I. (1994), Observations of the 1989–90 Redoubt Volcano eruption clouds using AVHRR satellite imagery, *U.S. Geol. Surv. Bull.* 2047:405–418.

Schneider, D. J., and Rose, W. I. (1995), Tracking of the 1992 Crater Peak/Spurr eruption clouds using AVHRR. *U.S. Geol. Surv. Bull.* 2139:27–36.

Schneider, D. J., Rose, W. I., Coke, L. R., Bluth, G. J. S., Sprod, I. E., and Krueger, A. J. (1999), Early evolution of a stratospheric volcanic eruption cloud as observed with TOMS and AVHRR. *J. Geophys. Res. Atmospheres* 104 (ND4):4037–4050.

Self, S., and Sparks, R. S. J. (1978), Characteristics of widespread pyroclastic deposits formed by the interaction of silicic magma and water. *Bull. Volcanol.* 41:196–212.

Self, S., and Walker, G. P. L. (1994), Ash clouds: characteristics of eruption columns. *U.S Geol. Surv. Bull.* 2047:65–73.

Simpson, J. J., and Al-Rawi, L. (1996), The Tile and General Research Imaging System (TIGRIS). *IEEE Trans. Geosci. Remote Sens.* 34:149–162.

Sparks, R. S. J. (1986), The dimensions and dynamics of volcanic eruption columns. *Bull. Volcanol.* 48:3–15.

Sparks, R. S. J., and Wilson, L. (1976), A model for the formation of ignimbrites by gravitational column collapse. *J. Geol. Soc. London* 132:441–452.

Stamnes, K., Tsay, S. C., Wiscombe, W. J., and Jayaweera, W. (1988), Numerically stable algorithm for discrete-ordinate-method radiative transfer in multiple scattering and emitting layered media. *Appl. Opt.* 27:2502–2509.

Stunder, B. (1999), Volcanic ash encounter probabilities. In *Proceedings of the 79th Annual Meeting of the American Meteorological Society*, 10–15 January, Dallas, TX, American Meteorological Society, Boston, M.A., pp. 25–28.

Turner, J. S. (1979), *Buoyancy Effects in Fluids*, Cambridge University Press, Cambridge, 368 pp.

Volz, F. E. (1972), Infrared absorption by atmospheric aerosol substances. *J. Geophys. Res.* 77:1017–1031.

Weinreb, M. M., Jamieson, M., Fulton, N., et al. (1997), Operational Calibration of Geostationary Operational Environmental Satellite -8 and -9 Imagers and Sounders. *Appl. Opt.* 36:6895–6904.

Williams, H., and McBirney, A. R. (1979), *Volcanology*, Freeman, Cooper, San Francisco, CA, 397 pp.

Wilson, C. J. N. (1994), Ash-fall deposits from large-scale phreatomagnetic volcanism: Limitations of available eruption-column models. *U.S.Geol. Surv. Bull.* 2047:93–99.

Wilson, L. (1976), Explosive volcanic eruptions: III—Plinian eruption columns. *Geophys. J. Roy. Astron. Soc.* 45:543–556.

Wilson, L., Sparks, R. S. J., and Walker, G. P. L. (1980), Explosive volcanic eruptions: IV—The control of magma properties and conduit geometry on eruption column behavior. *Geophys. J. Roy. Astron. Soc.* 83:1829–1836.

Woods, A. W. (1988), The fluid dynamics and thermodynamics of eruption columns. *Bull. Volcanol.* 50:169–193.

Young, M. E., Miller, T. P., and Gamble, B. M. (1987), The 1986 eruptions of Augustine Volcano, Alaska: hazards and effects, *USGS Circular* 998:3–13.

Young, S., Sparks, R. S. J., Aspinall, W. P., et al. (1998), Overview of the eruption of Soufriere Hills Volcano, Montserrat, 18 July 1995–December 1997. *Geophys. Res. Lett.* 25: 3389–3392.